nature neuroscience

RESOURCE

https://doi.org/10.1038/s41593-019-0476-2

Immediate and deferred epigenomic signatures of in vivo neuronal activation in mouse hippocampus

Jordi Fernandez-Albert[1], Michal Lipinski[1,5], María T. Lopez-Cascales[1,5], M. Jordan Rowley[2,4,5], Ana M. Martin-Gonzalez[1,3], Beatriz del Blanco[1], Victor G. Corces[2] and Angel Barco[1*]

Activity-driven transcription plays an important role in many brain processes, including those underlying memory and epilepsy. Here we combine genetic tagging of nuclei and ribosomes with RNA sequencing, chromatin immunoprecipitation with sequencing, assay for transposase-accessible chromatin using sequencing and Hi-C to investigate transcriptional and chromatin changes occurring in mouse hippocampal excitatory neurons at different time points after synchronous activation during seizure and sparse activation by novel context exploration. The transcriptional burst is associated with an increase in chromatin accessibility of activity-regulated genes and enhancers, de novo binding of activity-regulated transcription factors, augmented promoter–enhancer interactions and the formation of gene loops that bring together the transcription start site and transcription termination site of induced genes and may sustain the fast reloading of RNA polymerase complexes. Some chromatin occupancy changes and interactions, particularly those driven by AP1, remain long after neuronal activation and could underlie the changes in neuronal responsiveness and circuit connectivity observed in these neuroplasticity paradigms, perhaps thereby contributing to metaplasticity in the adult brain.

Activity-dependent transcription is a key part of the neuronal response to synaptic stimulation and is essential for the transition from short- to long-term forms of neuronal plasticity[1,2]. As a result, its deregulation is an important feature of many neurological diseases that are associated with cognitive dysfunction[3]. This is the case for epilepsy, a severe neurological condition that predisposes the patient to recurrent unprovoked seizures or transient disruption of brain function due to abnormal and uncontrolled neuronal activity, and can lead to brain damage, disability and even death. Beyond this pathological setting, activity-dependent transcription is also thought to contribute to the changes in circuit connectivity and neuronal responsiveness that are necessary for memory formation[1,4]. Thus, it has been hypothesized that the formation of long-term memory, which requires the activation of tightly regulated transcriptional programs during learning, relies not only on synaptic changes but also on modifications in the chromatin of activated neurons[5,6]. These epigenetic changes may contribute to long-lasting or permanent changes in the expression and responsiveness of genes involved in synaptic function, thereby representing a type of genomic memory.

New sequencing techniques have unveiled novel processes that contribute to the complex transcriptional response to neuronal activation, such as activity-regulated intron skipping, double-strand breaks and the production of different species of noncoding RNAs, including enhancer (eRNAs) and extracoding RNAs (ecRNAs)[7–13]. Despite this progress, an integrated view of the transcriptional and epigenomic changes triggered by neuronal activation in vivo is still lacking, partially because of the special challenges derived from brain complexity and cellular heterogeneity[1]. For instance, we do not know whether the processes mentioned above, most of which have only been described in vitro, also occur in the brain of behaving animals. Moreover, the mechanisms that sustain the activity-driven transcriptional burst and the nature of the afore predicted genomic memory remain poorly understood.

Here, we introduce methods to efficiently profile the transcriptome and epigenome of defined neuronal populations in the adult brain. Using these methods, we were able to generate a high-resolution, multidimensional and cell-type-specific draft of transcriptional and chromatin alterations associated with neuronal activation in vivo for physiological (novel context exploration) and pathological (status epilepticus (SE)) conditions. Our genome-wide screens and analyses provide molecular insight into both the rapid changes in gene expression that are initiated after neuronal activity and the more enduring changes that may underlie processes such as epilepsy and memory formation.

Results

Nuclear tagging enables neuronal-specific genomic screens and reveals broad changes to the nuclear transcriptome after SE. To investigate the transcriptional and chromatin changes specifically occurring in forebrain principal neurons following activation, we produced mice in which the nuclear envelope of these neurons is fluorescently tagged[14] (Fig. 1a,b). This genetic strategy combined with fluorescence activated nuclear sorting (FANS) allowed us to isolate this neuronal nuclei type from adult brain tissue (Supplementary Fig. 1a–c). After FANS, sorted nuclei can be used in different applications, from nuclear RNA (nuRNA) quantification (Supplementary Fig. 1d) to chromatin immunoprecipitation (ChIP) (Supplementary Fig. 1e) and enzymatic treatments such as the assay for transposase-accessible chromatin (ATAC) (Supplementary Fig. 1f). FANS represents a substantial improvement over cell sorting because it prevents the stress response triggered by neuronal dissociation that can occlude activity-induced changes. Moreover, since our method does not require the use of antibodies against green

[1]Instituto de Neurociencias, Universidad Miguel Hernández-Consejo Superior de Investigaciones Científicas, Sant Joan d'Alacant, Alicante, Spain. [2]Department of Biology, Emory University, Atlanta, GA, USA. [3]Nencki Institute of Experimental Biology PAS, Warsaw, Poland. [4]Present address: Department of Genetics, Cell Biology and Anatomy, University of Nebraska Medical Center, Omaha, NE, USA. [5]These authors contributed equally: Michal Lipinski, María T. Lopez-Cascales, M. Jordan Rowley *e-mail: abarco@umh.es

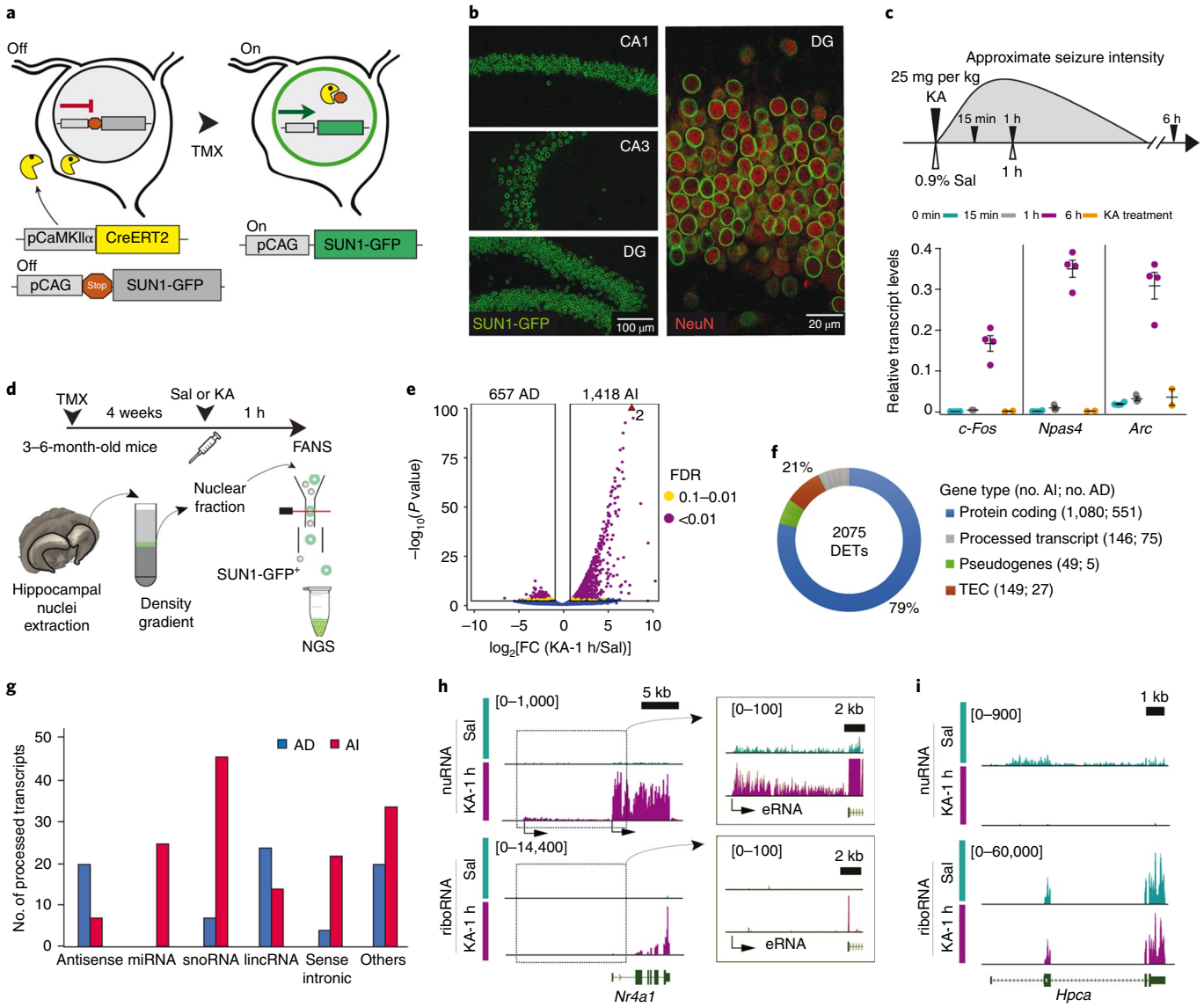

Fig. 1 | SE triggers broad changes in the nuclear transcriptome. a, Crossing of the tamoxifen (TMX)-inducible Cre-driver line CaMKIIα-creERT2 with mice that express SUN1-GFP in a Cre-recombination-dependent manner allows the tagging of the nuclear envelope in forebrain principal neurons for subsequent FANS-based isolation. **b**, Confocal images of principal hippocampal neurons in the CA1, CA3 and dentate gyrus (DG) subfields stained against GFP and the neuronal marker NeuN. Similar results were obtained in six independent experiments. **c**, Top: scheme depicting seizure strength and duration in KA-treated animals. Mice were injected with KA (25 mg per kg) and killed at various time points. $n = 4$ (0 min), 3 (15 min), 4 (1 h) and 2 (6 h) biologically independent samples. Bars indicate the mean ± s.e.m. As a reference, control mice were treated with saline (Sal) and killed 1 h after treatment. Bottom: RT–qPCR assays show transient IEG induction. **d**, Experimental design for KA-induced neuronal activity, nuclei isolation and application of next generation sequencing (NGS) techniques. **e**, Volcano plot showing the significance and *P* value distribution after differential gene expression analysis using DESeq2. AD, activity decreased; AI, activity induced. Sal: $n = 2$; KA-1 h: $n = 2$, biologically independent samples. Red arrowhead indicates the existence of two genes (*Fos* and *Fosb*) with $P < 1 \times 10^{-100}$. **f**, Transcript classification according to ENSEMBL for DETs 1 h after KA. TEC, to be experimentally confirmed. **g**, Number of processed transcript species detected for DETs 1 h after KA in the nuRNA-seq screens. miRNA, microRNA; snoRNA, small nucleolar RNA; lincRNA, long interspersed noncoding RNA. **h**, The nuRNA-seq screen detects activity-induced eRNA and other nucleus-resident noncoding RNAs. We also present the riboRNA-seq tracks for comparison. Values represent counts in RPM (reads per million). The arrows indicate transcript directionality. **i**, Genomic track for the gene encoding hippocalcin (*Hpca*), a calcium-binding protein that is highly expressed in the hippocampus and downregulated after SE. Values represent counts in RPM.

fluorescent protein (GFP), it can be combined with immunolabeling for secondary sorting to increase the specificity of the cellular population under investigation.

Exposure to the glutamate receptor agonist kainic acid (KA) is often used to model a single epileptic seizure episode—also known as SE—in experimental animals. SE evokes a strong transcriptional response in the hippocampus that includes the transient transcription of immediate-early genes (IEGs)[15,16] and rapid changes in chromatin marks and nuclear structure[17–20]. Nuclear-envelope-tagged mice were treated with 25 mg per kg of KA, which causes strong and synchronous activation in all the hippocampal subfields and leads to a robust but transient induction of IEGs (Fig. 1c). We used FANS to isolate nuRNA from hippocampal principal neurons of KA-treated mice and saline-treated mice (Fig. 1d;

Supplementary Fig. 1g). This screen detected more than 2,075 differentially expressed transcripts (DETs) (Fig. 1e; Supplementary Table 1), thus unveiling a broader impact and less skewed distribution than previous studies of activity-induced transcription[2]. We observed the induction of a rich variety of transcripts, including eRNAs and other nucleus-resident species (Fig. 1f–h). These profiles did not present the typical enrichment for 3′ sequences observed in mRNA sequencing and covered both exons and introns (Fig. 1h; Supplementary Fig. 1h). These results indicate that nuRNA sequencing (nuRNA-seq) is particularly well suited for studying dynamic transcriptional responses, because the signal precisely reflects the time point in which the transcripts are produced. As a result, nuRNA-seq provides a finer detection of activity-induced changes, particularly for transcripts that are already expressed in the basal state. It also unveils the transient downregulation of hundreds of transcripts (Fig. 1e,i), including many genes involved in basal metabolism (Supplementary Fig. 1i).

Compartment-specific transcriptomics reveals the uncoupling of the SE-induced neuronal transcriptome and translatome. Next, we used the same genetic approach to tag ribosomes and identify the pool of mRNAs that are translated in response to seizures (that is, the activity-induced neuronal translatome) (Fig. 2a–c; Supplementary Fig. 2a). Translating ribosomal affinity purification (TRAP)[21] led to an enrichment of neuron-specific transcripts and a depletion of glia-specific transcripts (Fig. 2d; Supplementary Fig. 2b). The sequencing (referred to as riboRNA-seq) and analysis of mRNAs isolated via TRAP retrieved 189 differentially translated genes (DTGs) (Fig. 2e; Supplementary Fig. 2c–e; Supplementary Table 2). Most of these DTGs encode proteins (Fig. 2f; Supplementary Fig. 2f) and relate to Gene Ontology (GO) functions such as "transcription cofactor activity", "kinase activity", "histone acetyltransferase" and "chromatin binding", and the nucleus was the most enriched cellular component (Supplementary Fig. 2g, red bars). Notably, the small set of activity-depleted mRNAs was also related to transcriptional regulation (Supplementary Fig. 2g, blue bars), which further underscores the importance of transcriptional and epigenetic regulation in activity-dependent processes.

The availability of neuronal-specific riboRNA-seq and nuRNA-seq data provides a unique opportunity for the dissection of RNA-related mechanisms that are involved in the response to activation. First, the comparison of the number, magnitude and distribution of the changes confirmed the special suitability of nuRNA-seq for transcriptional dynamics studies (Figs. 1h,i and 2g). Second, despite these differences, we observed a robust correlation between changes in both screens demonstrating the coordinated regulation of RNA transcription and export following neuronal activation (Fig. 2h). Third, we identified a small number of transcripts that escape the general correlation. These mRNAs showed an increase in riboRNA-seq profiles, but no change, or even a decrease, in nuRNA-seq profiles. This pattern suggests that activity-dependent regulation of these transcripts occurs at the translational rather than at the transcriptional level (Fig. 2i; Supplementary Fig. 2h, discordant). Notably, some of these genes are known to be post-transcriptionally regulated in other cell types[22]. This is the case for *Nfkbiz* (Fig. 2j), which encodes an atypical member of the nuclear factor-κB (NF-κB) family and harbors a translational silencing element in the 3′ untranslated region that destabilizes the mRNA[23,24]. Fourth, we observed striking differences in the transcription termination site (TTS) of IEG transcripts obtained after nuclear and ribosome-bound RNA isolation (Fig. 2k; Supplementary Fig. 2i). The nuclear transcripts were consistently longer, extending several hundred base pairs after the annotated TTS (Fig. 2k, red bar). This observation indicates that activity-induced ecRNAs, which have been postulated to prevent gene inactivation in embryonic neuronal cultures[8], are also produced in the adult brain. Overall, these findings underscore the value of parallel compartment-specific transcriptome analyses to unveil novel regulatory mechanisms.

The activity-induced transcriptional burst causes a dramatic increase in chromatin accessibility at IEGs. To precisely correlate the transcriptional differences with changes in chromatin occupancy and transcription factor (TF) binding, we next assessed chromatin accessibility by ATAC and sequencing (ATAC-seq)[25]. The combination of FANS and ATAC-seq revealed that the chromatin accessibility profile of hippocampal neurons (Supplementary Fig. 3a–c) is dramatically altered during SE (Fig. 3a). The differential accessibility screen retrieved more than 30,000 differentially accessible regions (DARs) (Fig. 3b; Supplementary Table 3a), thus providing a deeper survey of activity-dependent changes than previous analyses[26] (Supplementary Fig. 2d–f). While a KA-induced increase of chromatin accessibility was primarily observed within gene regions, particularly within close proximity to the TSSs (<1 kb), modest chromatin closing occurred more frequently at intergenic regions (Supplementary Fig. 2g). Overall, the most prominent changes in chromatin accessibility corresponded to the opening of gene regions (Fig. 3c).

We next used binding and expression target analysis (BETA) to integrate ATAC-seq and RNA-seq data[27] and found that the increase in chromatin accessibility throughout the gene body is an excellent predictor of transcriptional activation ($P < 3.86 \times 10^{-36}$, Supplementary Fig. 4a). ATAC-seq data correlated with changes in the riboRNA-seq and nuRNA-seq screens (Supplementary Fig. 4b), but the correlation was stronger and depended on more genes in the case of nuRNA-seq (Supplementary Fig. 4c; Supplementary Table 3b). These comparisons revealed a very prominent increase in accessibility at the gene body of activity-induced genes that extended beyond the TTS and narrowly matched transcript production (Fig. 3d). We next investigated the relationship between changes in accessibility, transcription and RNA polymerase II complex (RNAPII) binding. Experiments using neuronal cultures have suggested that IEGs may have pre-assembled RNAPII at the TSS in the basal state[28]. RNAPII poising is not, however, evident in vivo. Although we detected a modest presence of RNAPII at the promoter of rapid response genes in saline-treated mice, SE triggered a robust de novo binding (Fig. 3d). Nucleosome positioning at the TSS of activity-regulated genes showed a shift of the +1 nucleosome in activity-induced genes, which also reflected the de novo entrance of RNAPII[29] (Fig. 3e). In addition to promoter binding, neuronal activation increased RNAPII occupancy of the gene body and the TTS in activity-regulated genes, which matched the production of extended nuclear transcripts (Fig. 3d,f) and enhanced intragenic accessibility (Supplementary Fig. 4d). These results suggest that the enhanced accessibility at IEGs reflects the continuous passage of the RNAPII. To assess this hypothesis, we examined the effect of triptolide (TPL), a drug that inhibits transcription initiation[30,31], on chromatin accessibility changes (Fig. 3g). Both IEG induction (Supplementary Fig. 4e) and increased accessibility in the gene body of upregulated genes (Fig. 3f; Supplementary Table 3c) were reduced in animals treated with TPL before KA administration. The impact of TPL on DARs was more prominent in the genes that showed the largest changes (Supplementary Fig. 4f) and stronger in gene bodies than TSSs (Supplementary Fig. 4g), thereby confirming that most of these changes are directly derived from the traffic of RNAPII during the transcriptional burst. Administration of TPL also prevented the nucleosome shift at the TSS caused by the entry of new RNAPII complexes (Fig. 3e, orange violins). Interestingly, our analyses showed that about 30% of the regions with altered accessibility in response to KA were not affected by TPL (Fig. 3g,h), thus indicating that other mechanisms, such as the de novo binding of activity-regulated TFs and the recruitment of co-activators, also contribute to activity-dependent changes in the chromatin.

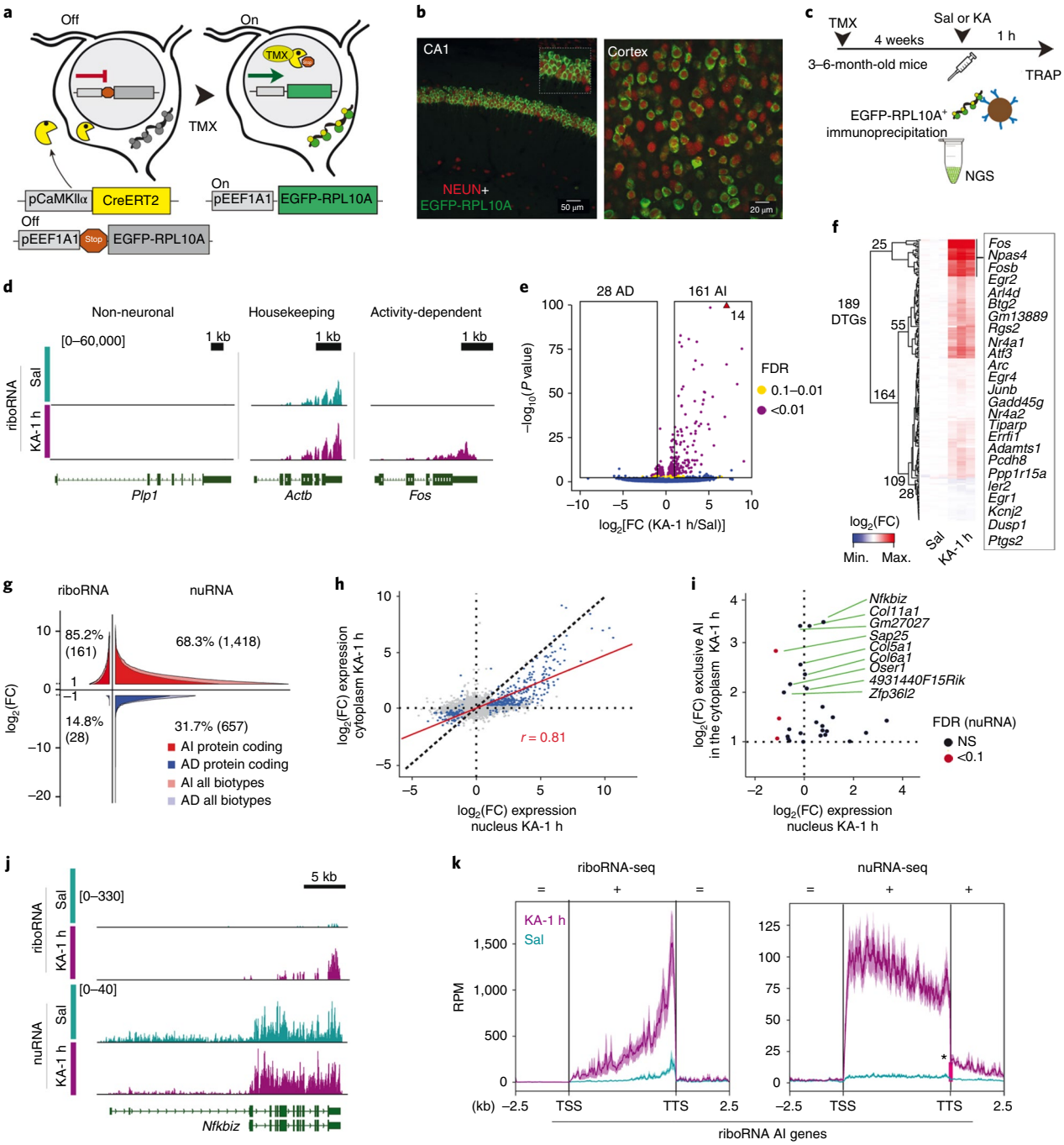

Fig. 2 | Compartment-specific transcriptomics reveals changes in neuronal transcript production and translation. a, Crossing the TMX-inducible Cre-driver line CaMKIIα-creERT2 with mice that express enhanced GFP (EGFP)-RPL10A in a Cre-recombination-dependent manner allows the tagging of ribosomes in forebrain principal neurons for subsequent immunoprecipitation-based isolation. **b**, Confocal images of principal neurons in the CA1 subfield and cortex stained against GFP and the neuron marker NeuN. Similar results were obtained in three independent experiments. **c**, Experimental design for KA-induced neuronal activation and ribosomal RNA isolation. **d**, Genomic snapshots for representative examples of glia-specific (*Plp1*), housekeeping (*ActB*) and activity-induced (*Fos*) genes. Values indicate the levels of counts in RPM. **e**, Volcano plot showing the significance and *P* value distribution after differential transcript abundance analysis using DESeq2. Sal: $n=3$, KA-1 h: $n=3$, biologically independent samples. Red arrowhead indicates the existence of 14 genes with $P < 1 \times 10^{-100}$. **f**, Heatmap of FCs in DTGs retrieved in the riboRNA-seq screen. **g**, Density distribution of DTGs and DETs in the riboRNA-seq and nuRNA-seq screens, respectively. Colors indicate the distribution of protein-coding RNAs versus all other biotypes. **h**, Correlation of FC values for genes significantly regulated (FDR < 0.1, 372 genes) in both datasets (blue). All other detected genes are labeled in gray. Cytoplasm: Sal: $n=3$, KA-1 h: $n=3$; nucleus: Sal: $n=2$, KA-1 h: $n=2$, biologically independent samples. Pearson's correlation index is shown. **i**, Scatter plot of $\log_2$(FC) for genes exclusively upregulated in the cytoplasm (FDR < 0.1; Sal: $n=3$, KA-1 h: $n=3$, biologically independent samples) and FC values in the nucleus (colors indicate the FDR significance in nuRNA-seq analysis: not significant (NS): FDR > 0.1 in nuRNA-seq; Sal: $n=2$; KA-1 h: $n=2$, biologically independent samples). **j**, Comparison of nuRNA-seq and riboRNA-seq tracks in *Nfkbiz*. The vertical scale shows counts in RPM. **k**, Metagene mapability profiles for riboRNA-seq (Sal: $n=3$, KA-1 h: $n=3$) and nuRNA-seq (Sal: $n=2$, KA-1 h: $n=2$) samples at genes upregulated in both datasets. The asterisk and red bar in the right graph indicate the significant difference downstream of the TTS in nuRNA-seq. The unbroken lines indicate the mean and the shaded lines indicate s.e.m.

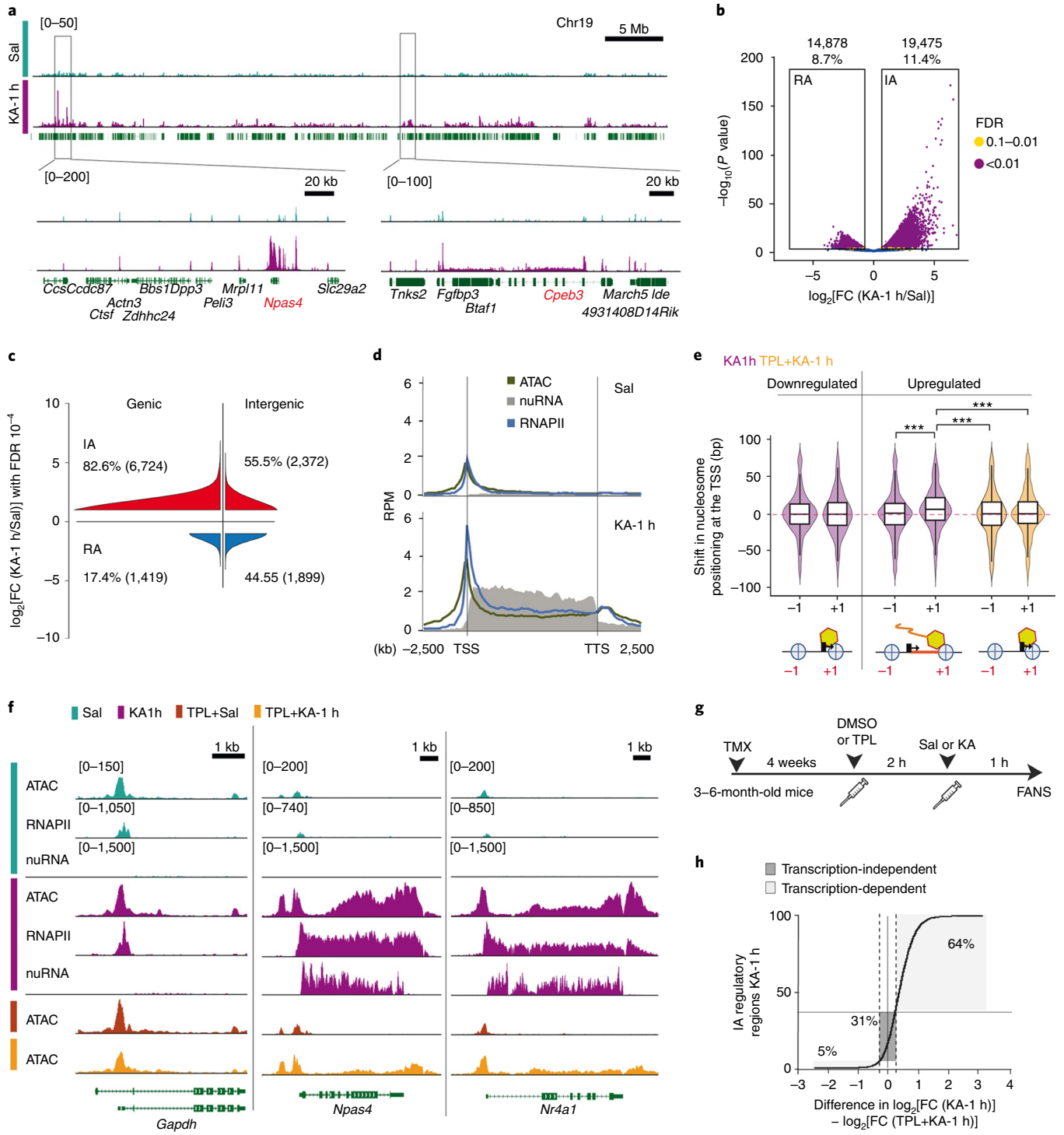

Fig. 3 | Neuronal activation causes a dramatic increase in accessibility at activity-regulated genes associated with the transcriptional burst. a, Genomic profile at the chromosome 19 (Chr19) locus containing the activity-induced genes *Npas4* and *Cpeb3* (red). **b**, Volcano plot showing the significance value distribution after DAR analysis using DESeq2; upper values indicate number of regions and percentage of all the accessible regions detected. RA, reduced accessibility; IA, increased accessibility. Sal: $n=2$, KA-1 h: $n=2$, biologically independent samples. **c**, Density distribution of highly significant intragenic and intergenic DARs (FDR $<10^{-4}$) after DESeq2 analysis. Sal: $n=2$, KA-1 h: $n=2$. Values obtained by DESeq2 analysis. **d**, Metagene plot for ATAC-seq (Sal: $n=2$, KA-1 h: $n=2$), RNAPII ChIP-seq (Sal: $n=1$, KA-1 h: $n=1$) and nuRNA-seq signals at upregulated genes 1 h after saline or KA administration retrieved by DESeq2 analysis. $\log_2(FC)>3$; FDR <0.1; Sal: $n=2$, KA-1 h: $n=2$. **e**, Violin plot showing the shift in the distribution of nucleosome positioning at the TSS of downregulated and upregulated genes 1 h after KA or after TPL+KA-1 h treatment. The boxplot indicates the median, interquartile range and minimum and maximum. The broken red line indicates no shift at 0. KA-1 h: $n=2$, TPL+KA-1 h: $n=1$. ***P-adjusted <0.00001 in post hoc Dunn test for Kruskal–Wallis with multiple comparisons. The schematic beneath the violin plots represents the displacement of the +1 nucleosome by the RNAPII complex (yellow hexagon) in upregulated genes. **f**, Top: genomic snapshots of ATAC-seq, nuRNA-seq and RNAPII-ChIP-seq profiles in control and activity-regulated genes 1 h after saline or KA administration. Bottom: impact of TPL on ATAC-seq profiles. Values indicate the levels of counts in RPM. **g**, Experimental design for the TPL blockade of KA-induced changes. DMSO, dimethylsulfoxide. **h**, Distribution of the difference of $\log_2(FC)$ for KA-1 h and TPL+KA-1 h at the DARs detected in KA-1 h. The DARs considered to be transcription-independent ($\log_2(FC)$ difference smaller than ±0.25) occupy the gray box.

TF and transcriptional co-activator binding at activity-regulated enhancers. Similar to TSSs and intragenic sequences (Fig. 3d), SE-induced changes at extragenic regions (>1 kb from the gene body) also correlated with transcriptional changes in the proximal genes (Supplementary Fig. 5a). To explore these changes in greater detail, we classified the accessible extragenic regions in the chromatin of mature excitatory neurons into promoters and putative enhancers and distinguished between regions with a stronger or weaker epigenetic signature (Fig. 4a). Promoters were characterized by the prominent presence of RNAPII and trimethylation of histone H3 at lysine 4 (H3K4me3) together with a depletion of monomethylation of histone H3 at lysine 4 (H3K4me1). In contrast, putative enhancers presented enrichments for the histone post-translational modifications H3K4me1 and acetylation of H3 at lysine 27 (H3K27ac) together with binding of the transcriptional co-activator and lysine acetyltransferase CREB-binding protein (CBP). About 10% of these promoter regions and 25% of the putative enhancer regions showed changes in accessibility during SE (Supplementary Fig. 5b). Notably, these changes were consistent with ChIP-seq profiles for the binding of RNAPII and CBP following SE, thus indicating that the changes are driven by the activity-dependent recruitment of transcriptional complexes. While promoters and strong enhancers showed robust activity-dependent binding of both RNAPII and CBP, weak enhancers only showed CBP binding (Supplementary Fig. 5c), which indicates that they may be poised for activation[32]. Consistent with this view, we detected an activity-dependent increase in H3K27ac at the same sites (Supplementary Fig. 5d) in primary cultures of embryonic cortical neurons stimulated with KCl[33]. Furthermore, activity-dependent CBP recruitment and increased H3K27ac occurred at both TPL-sensitive and TPL-resistant sites (Supplementary Fig. 5e–f), which suggests that CBP recruitment and enhancer activation may be independent of RNAPII action. Intriguingly, 75% of the activity-induced transcripts were associated with activity-driven changes in accessibility (Fig. 4b; Supplementary Fig. 5g), but only 25% of the promoters and 10% of the enhancers that displayed increased accessibility were linked to activity-induced transcripts (Supplementary Fig. 5h). This discrepancy indicates that synaptic activity triggers a large number of chromatin changes that are not directly associated with transcription of the nearest gene.

We next investigated the abundance of TF binding sites at accessible regions that show a significant increase, reduction or no change in accessibility following SE. The promoters and enhancers showing an increase in accessibility were enriched for motifs recognized by TFs that are involved in neuronal plasticity processes; such TFs included AP1 (TRE) and CREB (CRE)[2]. In turn, the promoters and enhancers displaying reduced accessibility showed enrichment for motifs associated with neuronal identity, such as NEUROD1 (Fig. 4c). This result again points to a competition between activity-regulated genes and other highly expressed neuronal genes for the basal transcription machinery. Interestingly, constitutive promoters and enhancers were both enriched in CTCF binding sites, which suggests that the general architecture of the chromatin in neurons is not severely altered following activation. To directly assess the occupancy of these sites before and during SE, we analyzed their digital footprints in ATAC-seq profiles (Fig. 4d). Occupancy by the activity-regulated TFs CREB, SRF, AP1 and MEF2C was detected in promoter and enhancer regions. While the footprint for the CREB family members was stronger in promoters than in enhancers, the footprints for AP1 and MEF2C presented the opposite pattern (Fig. 4e–f). After SE, constitutive-activity-regulated TFs, such as SRF and CREB, did not show large changes in their footprint, although we detected some de novo binding at enhancer regions (Fig. 4f–g; Supplementary Fig. 6a). In contrast, AP1 showed a robust increase in occupancy at enhancer regions (Fig. 4f–g; Supplementary Fig. 6a) that, consistent with the de novo synthesis of AP1 proteins, was highly sensitive to TPL (Supplementary Fig. 6b,c). ChIP-seq data for CREB, SRF and Fos in cortical neurons demonstrated the occupancy of these sites by the corresponding TFs after KCl stimulation[7,33], thus suggesting that both modes of activation trigger the same genomic mechanisms (Supplementary Fig. 6d). Consistent with the recently postulated role of the acquisition of signal-regulated DNA elements in gene regulatory regions in the evolution of cognitive abilities[34], these footprints are evolutionarily conserved (Supplementary Fig. 6e).

Physiological and pathological neuronal activation share common mechanisms but trigger distinct epigenomic signatures. To investigate whether the genomic events described above are exclusive to pathological neuronal overactivation or can also be observed after neuronal activation in physiological conditions, we next explored chromatin changes triggered by the exploration of a novel and rich spatial context. This experience is known to induce IEG transcription in sparse neuronal assemblies in the hippocampus of rodents[35] (Fig. 5a; Supplementary Fig. 7a). Nuclear-envelope-tagged mice were subjected to novelty exploration (NE) for 1 h. We then used FANS and Fos immunostaining to isolate the small percentage of neuronal nuclei responding to this experience (25,000 $SUN1^+$and Fos^+ nuclei from the hippocampi of 6 novelty-exposed mice; Fig. 5b and Supplementary Fig. 7b). We also isolated the same number of $SUN1^+$ and Fos^- nuclei for a direct comparison of activated and non-activated neurons from the same animal. Both types of nuclei were processed for ATAC-seq to produce a map of learning-related chromatin accessibility changes. Although the comparison of Fos^+ and Fos^- neurons revealed fewer numerous and more modest changes (Fig. 5c; Supplementary Fig. 7c; Supplementary Table 4), there was a large overlap between the NE- and SE-induced DARs. A principal component analysis showed that Fos^+ nuclei clustered with the KA-1 h samples, while Fos^- nuclei clustered with the samples of saline-treated mice (Supplementary Fig. 7d,e). Similar to our SE study, chromatin accessibility changes in gene bodies correlated with nuclear transcript induction following NE[36] (Supplementary Fig. 7f), and digital footprinting revealed a clear enrichment for AP1 and MEF2C binding at activity-regulated enhancers, albeit fewer TF motifs were detected in the NE scenario than in SE (Fig. 5d).

Although most of the genes responding to NE at the chromatin accessibility and transcriptional levels were retrieved during SE, a subset of genes was unique to this paradigm (Fig. 5e). Consistently, GO enrichment analyses revealed a greater enrichment for neuronal plasticity and memory functions in the NE-specific set, while the SE-specific genes were related to the modification and processing of RNA and protein, including the regulation of Tau and kinases involved in neurophysiopathology[37] (Fig. 5f). The comparison of chromatin accessibility profiles also revealed notable differences between SE and NE (Supplementary Fig. 7c and compare Supplementary Figs. 7g and 5h). For instance, the TF footprints detected at DARs exclusive to the NE situation did not show de novo RNAPII or CBP binding after SE (Supplementary Fig. 7h). However, the same sites displayed reduced DNA methylation and enhanced H3K4me1 and H3K27ac (two histone post-translational modifications associated with enhancer activation) after fear conditioning in a new context[38] (Supplementary Fig. 7i). These results underscore both the common mechanisms and the stimuli-dependent differences in the genomic signature of pathological versus physiological activation of principal neurons.

Longitudinal analyses unveil chromatin changes that remain long after SE. Next, we investigated the duration and reversibility of the transcriptional and chromatin accessibility changes triggered by neuronal activation. To this end, we expanded our study of the epigenetic and transcriptome signature of synchronous hippocampal neuron activation to 6 h and 48 h after SE. In the case of

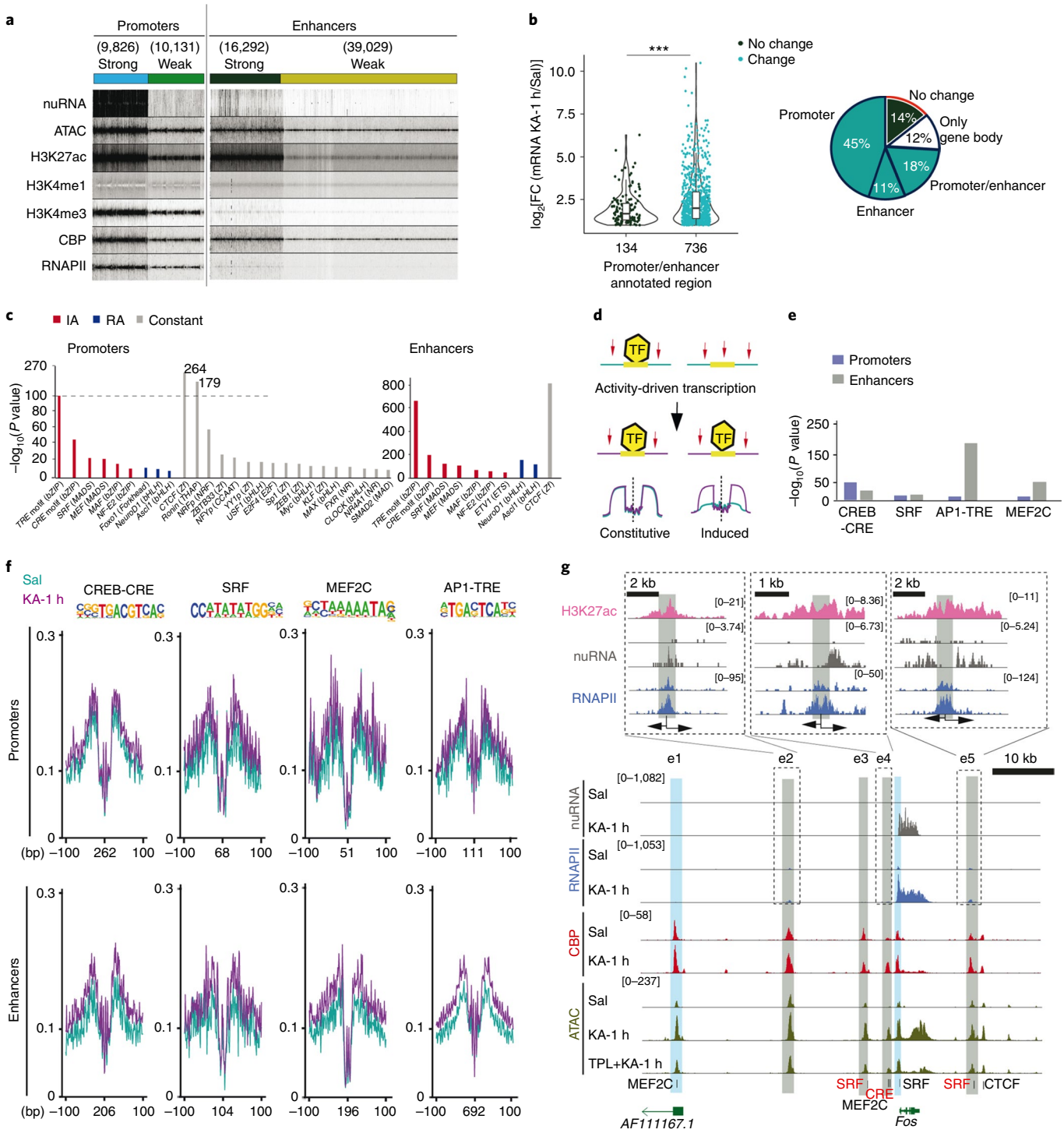

Fig. 4 | Neuronal activation induces TF binding at extragenic sites. a, *K*-mean clustering for accessible extragenic regions (±5 kb) generated using the profiles of ATAC-seq, nuRNA-seq and ChIP-seq for RNAPII, CBP, H3K27ac, H3K4me3 and H3K4me1 in hippocampal chromatin of naive animals (this study and data from other studies[49,50]). **b**, Left: violin plot showing the $\log_2$(FC) distribution and the number of upregulated nuclear transcripts with promoter and enhancer annotations that change or do not change during SE. The boxplot indicates the median, interquartile range and minimum and maximum. Sal: $n=2$, KA-1 h: $n=2$; ***P-adjusted value $=2.10^{-16}$ in the Kruskal–Wallis test. Right: the sector graph shows the percentage of regions according to their annotation and change following SE. **c**, Motif enrichment after HOMER analysis at detected promoter and enhancer accessible regions from RA, IA and constant regions. Sal: $n=2$, KA-1 h: $n=2$. **d**, Scheme of digital footprinting analysis. Red arrows indicate sites accessible to tn5 cutting. Occupied TF-binding sites are more protected than the immediate surrounding regions. **e**, Motif enrichment significance after HOMER analysis at detected footprints in IA promoters and enhancers. Sal: $n=2$, KA-1 h: $n=2$. **f**, Digital footprinting at enriched motifs and number of motifs detected (values correspond to normalized tn5 insertions). **g**, As an example, the snapshot shows nuRNAs, ATAC-seq, RNAPII and CBP binding at regions flanking *Fos* in saline, KA-1 h and TPL+KA-1 h samples (values in RPM). Annotations label the detected footprints (in red, less stringent footprints) and classification for the regions (blue, promoters; gray, enhancers). The upper insets zoom on enhancers with detected eRNAs. Arrows indicate transcript directionality.

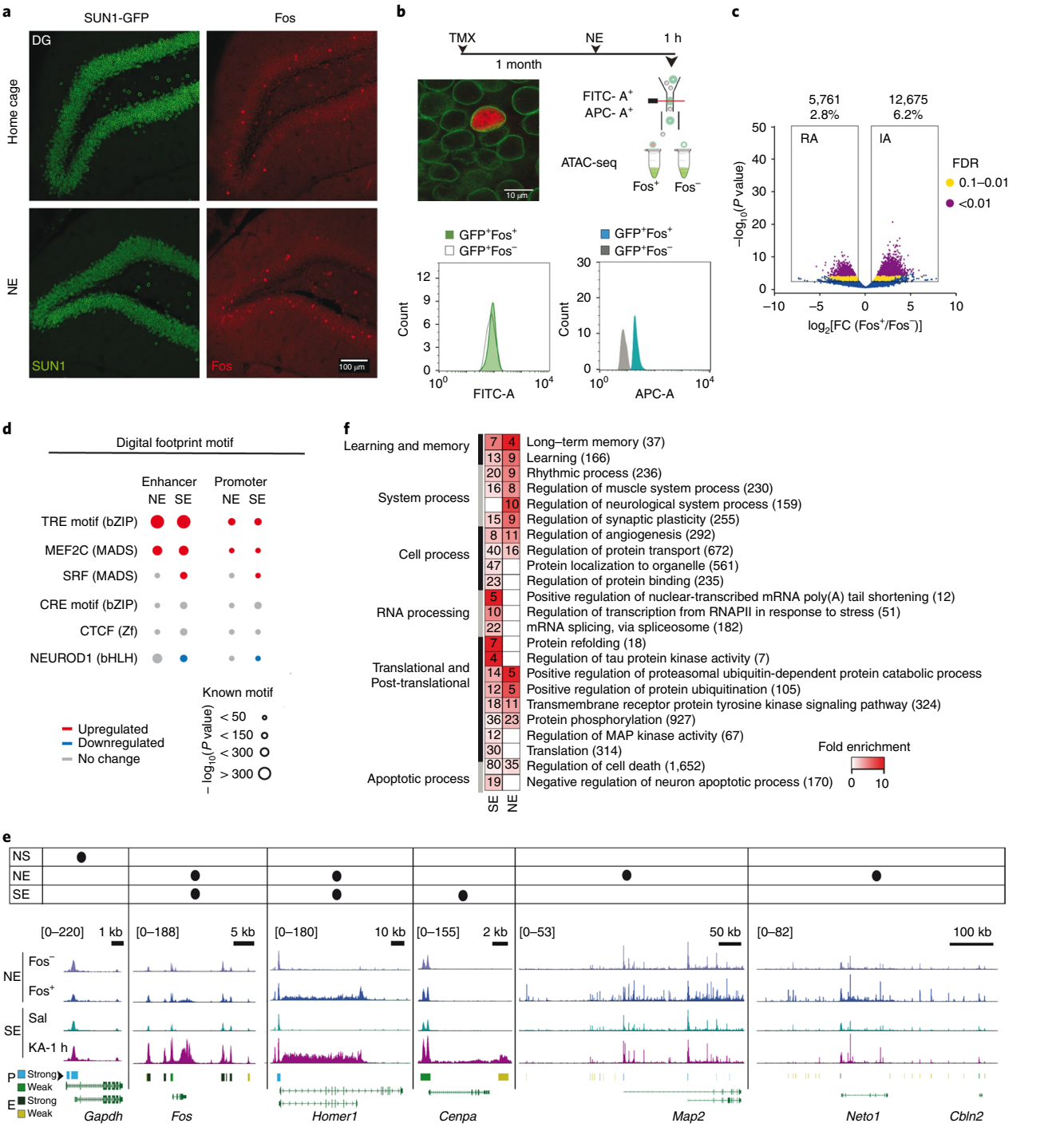

Fig. 5 | Physiological and pathological neuronal activation share common mechanisms but trigger distinct genomic signatures. a, Confocal images of granular neurons in the DG of mice maintained in their home cages or exposed to 1 h of NE. Brain slices were stained against GFP and Fos. Similar results were obtained in three independent experiments. **b**, Experimental design of the approach used to study chromatin changes in neurons activated by 1 h of NE. Bottom: channel filtering of the flow cytometry signal for SUN1-GFP$^+$ (fluorescein isothiocyanate (FITC)-A) singlet nuclei and differences in Fos staining (APC-A). Similar results were obtained in three independent experiments. **c**, Volcano plot showing the significance value distribution after differential accessible regions analysis; upper values indicate the number of regions and percentage of all the accessible regions detected. Fos$^-$: $n=1$, Fos$^+$: $n=1$, directly related (obtained from the same animals) samples. Values obtained after DESeq2 analysis including in the experiment design the comparisons with KA-1 h and saline condition to support the reduced n for value transformations. **d**, Digital footprinting at enhancer and promoter sites in NE and SE, indicating the motif enrichment (circle size) and the associated TF expression change in NE (from a previous study[36]) and SE (this study) nuRNA-seq datasets. **e**, Comparison of ATAC-seq tracks for physiologically (Fos$^+$ versus Fos$^-$ neurons) and chemically activated (saline versus KA-1 h) neurons at the DEG in the SE (this study) and NE[36] nuRNA-seq datasets. The table indicates the increase in accessibility at the gene body and nuRNA upregulation per each condition. Lower bars indicate the regions classified as strong or weak at promoters (P) and enhancers (E). Values indicate the levels of counts in RPM. **f**, Heatmap of fold enrichment for biological process GO terms in genes displaying increased accessibility in the NE and SE datasets. Values in parentheses correspond to the number of genes associated with each term.

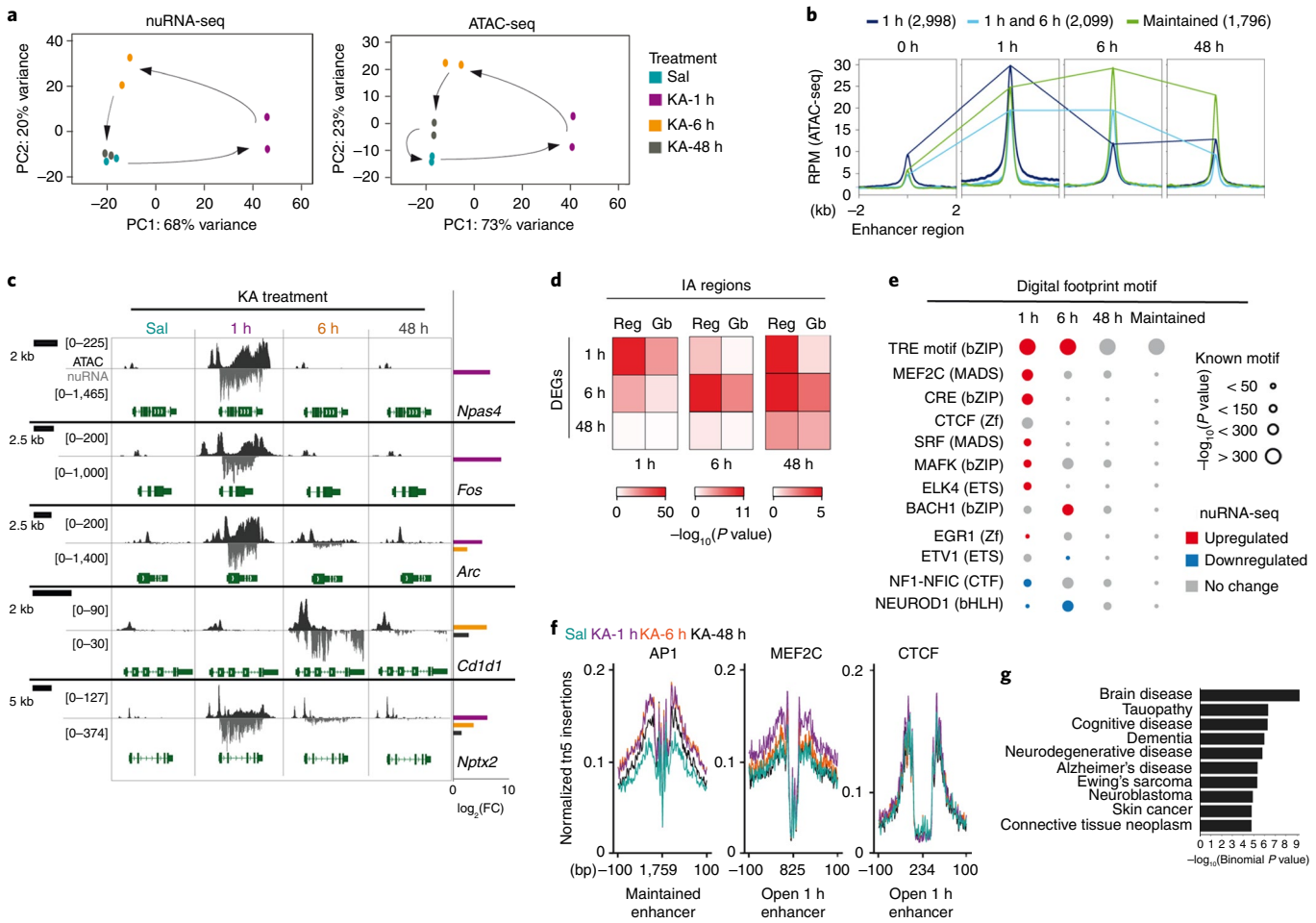

Fig. 6 | Long-lasting chromatin accessibility changes are associated with AP1 binding and disease. a, Principal component (PC) analysis for nuRNA-seq (left) and ATAC-seq (right) datasets. Saline and KA-48 h samples overlap distant from KA-1 h samples. The separation of KA-6 h samples suggests an independent second wave of transcriptional changes (Sal: $n=2$, KA-1 h: $n=2$, KA-6 h: $n=2$, KA-48 h: $n=2$; same number of biologically independent samples in ATAC-seq and nuRNA-seq). **b**, ATAC-seq signals at activity-regulated enhancers that show IA exclusively at 1 h, at 1 h and 6 h, or maintained for 48 h. **c**, Snapshots for ATAC-seq and nuRNA-seq tracks at the different time points. The examples illustrate the diversity of profiles under the general denomination of IEG. *Fos* and *Npas4* present a very rapid and transient induction associated with dramatic changes in the accessibility of the chromatin at the gene body, while other IEGs, such as *Arc* and *Nptx2*, maintain their induction for hours or even days after SE. Late-response genes, such as *Cd1d1*, increase transcription and chromatin accessibility long after SE. Right bars show significant (FDR < 0.1) $\log_2$(FC) for nuclear transcripts after DESeq2 analysis at each time point (Sal: $n=2$, KA-1 h: $n=2$, KA-6 h: $n=2$, KA-48 h: $n=2$; same number of biologically independent replicates in ATAC-seq and nuRNA-seq). Values are shown in RPM. **d**, Heatmap showing the significance after BETA analysis for IA regions and transcript levels in each time point at promoter and enhancer (Reg) and gene bodies (Gb) (Sal: $n=2$, KA-1 h: $n=2$, KA-6 h: $n=2$, KA-48 h: $n=2$; same number of biologically independent replicates in ATAC-seq and nuRNA-seq). **e**, Digital footprinting at enhancer/promoter sites in SE dynamics, indicating the motif enrichment (circle size) and the associated TF expression change in NE nuRNA-seq datasets. **f**, Footprinted AP1, MEF2C and CTCF sites at 0 h, 1 h, 6 h and 48 h after KA detected on enhancer DARs presenting increased accessibility during SE (open 1 h) and maintained from 1 to 48 h. The number of motifs detected is indicated below the graph. **g**, Genes associated with the enhancer-overlapping DARs that show a maintained increase in accessibility are disease-related (Sal: $n=2$, KA-1 h: $n=2$, KA-6 h: $n=2$, KA-48 h: $n=2$).

nuRNA-seq, the longitudinal analysis revealed a dynamic scenario in which the broad initial transcriptional response led to a secondary wave of changes at 6 h that still affected thousands of transcripts, but with more moderate changes, while 48 h after SE, the neuronal transcriptome was largely restored to the basal situation (Fig. 6a; Supplementary Fig. 8a–d; Supplementary Table 5). Of note, there were more genes that were downregulated than upregulated at later time points, which contrasts with the oppositely skewed distribution observed during SE. Some of these downregulated genes were related to potassium and calcium transport, likely reflecting the late homeostatic response (Supplementary Fig. 8e).

In contrast, the longitudinal analysis of chromatin accessibility changes (Supplementary Table 6) did not reveal the same restoration to the original state. The samples corresponding to 48 h after KA approached the control samples (saline), but did not overlap (Fig. 6a). Indeed, a relatively large subset of DARs (>10,000), particularly those located at intergenic regions, persisted 48 h after SE (Fig. 6b,c; Supplementary Fig. 8f–i). Moreover, although BETA revealed a clear correlation between augmented transcript production and accessibility for each time point (Fig. 6d), the extragenic regulatory regions exhibiting increased accessibility at 48 h showed a better correlation with transcriptional changes at 1 h and 6 h than at 48 h.

The digital footprint analysis at those regions displaying long-lasting changes revealed a specific enrichment for AP1 binding, while the enrichment for other activity-regulated TFs, such

as MEF2C, was only detected at earlier time points (Fig. 6e,f). Notably, AP1 sites also show stable accessibility changes after electrical stimulation of dentate gyrus neurons[26]. ChIP-seq data for Fos binding following KCl stimulation of cortical neurons[7,33] was consistent with the occupancy of these sites (Supplementary Fig. 9a). Interestingly, the AP1 sites presenting long-lasting changes after SE also responded to NE (Supplementary Fig. 9b), which further underscores the biological relevance of these sites. This binding signal might correspond to Fos–Jun dimers or to other TFs of the same family that recognize the same motif[26]. Although the activity-induced transcription of *AP1* genes is highly transient (Fig. 6e), at the protein level, Fos immunoreactivity persists even 6 h after SE (Supplementary Fig. 9c). Therefore, we cannot discard the possibility that a reduced number of AP1 molecules induced during seizure could still remain bound at specific loci at later time points. Notably, the genomic regions displaying long-lasting changes were associated with genes involved in brain diseases related to protein accumulation (Fig. 6g), thus linking these changes with pathological traits. Consistent with this notion, mice that underwent SE displayed both memory deficits (Supplementary Fig. 9d) and impaired induction of *Fos* (Supplementary Fig. 9e) when subjected to a novel object location memory task (which is known to be hippocampal-dependent). The *Fos* locus was surrounded by several regions that displayed long-lasting changes in occupancy, including sustained AP1 binding at putative enhancers located close to the neighboring gene *Jdp2* (Supplementary Fig. 9f), which encodes a repressor of AP1. These results suggest that the 'silent' changes retrieved in our longitudinal study might affect the future responsiveness of the neuron and thereby contribute to hippocampal dysfunction in the epileptic brain.

Activity-driven transcription is associated with the formation of gene loops and stronger promoter–enhancer interactions. Our multi-omic analysis indicated that activity-driven transcription is associated with a rapid increase in chromatin accessibility and RNAPII occupancy that extends over the gene limit and pointed to the participation of structural proteins that topologically delimit locus responsiveness. In addition, we detected a delayed response in the form of long-lasting changes in chromatin occupancy that suggest the existence of a genomic memory in the form of protein binding or architectural modifications. To test these hypotheses, we investigated the three-dimensional chromatin architecture of activated hippocampal neurons 1 h and 48 h after SE using Hi-C (Supplementary Fig. 10a). This genome-wide and fully unbiased chromatin conformation capture technique enables the analysis of compartments, CTCF loops and gene loops[39]. We combined our FANS procedure with Hi-C to generate a draft of DNA interactions in 25-kb bins for excitatory neurons of adult behaving mice both in the basal situation and during SE (Fig. 7a). Compartments were generally similar to those reported for cortical neurons differentiated in vitro[40] (Supplementary Fig. 10b). Furthermore, changes in gene expression during neuronal differentiation correlated with similar changes to compartments in these in vitro differentiated neurons and adult neuronal tissue (Supplementary Fig. 10c,d).

We then searched for after-activity-regulated CTCF loops using HiCCUPS[41]. We detected differences in CTCF loops between embryonic stem cells[40], in vitro differentiated neurons[40] and adult principal neurons; however, we did not detect significant activity-driven changes, thus suggesting that CTCF loops are largely invariant during neuronal activation (Supplementary Fig. 10e,f). This lack of change is consistent with our TF-binding site enrichment and digital footprint analyses (Fig. 4c; Supplementary Fig. 6c). Nevertheless, we detected changes in the interactions of activity-induced genes with nearby DARs (Supplementary Fig. 10g). The differences in the compartmental eigenvector strongly correlated with the observed increase in the transcription of activity-regulated genes 1 h after KA treatment (Fig. 7b, purple boxes). To test this on a genome-wide scale, we used Fit-Hi-C to retrieve a list of significantly enriched pairwise intrachromosomal interactions (Supplementary Table 7). Our analyses revealed enhanced interactions between proximal extragenic DARs and the TSS of activity-induced genes (Fig. 7c), such as the IEG *Fos* (Fig. 7d), and between the TSS and TTS of activity-induced genes (Fig. 7e,f). We then evaluated the appearance of gene loops between the TSS and TTS of genes with high levels of nuRNA-seq signals and found increased formation following SE (Supplementary Fig. 10h). These gene loops between the TSS and the TTS of strongly induced genes (Fig. 7g and Supplementary Fig. 10i show *Bdnf* as an example) may be essential for supporting the fast transcriptional rate of these loci. Their detection, together with the robust increase in gene body accessibility and intragenic

Fig. 7 | Neuronal activation induces gene loops and strengthens TSS–enhancer interactions. a, Hi-C maps of normalized distances in chromatin samples of saline-treated mice and KA-treated mice 1 and 48 h after drug administration. Note the segregation of active and inactive chromatin in both situations, represented by positive and negative eigenvectors at the top and the augmented inflection in a SE-induced locus. **b**, Difference in the compartmental eigenvector 1 h or 48 h after KA treatment compared to saline at genes with increased expression 1 h after KA treatment as retrieved by DESeq2. Hi-C, Sal: $n=2$, KA-1 h: $n=2$, KA-48 h: $n=2$; nuRNA-seq, Sal: $n=2$, KA-1 h: $n=2$ biological replicates. The boxplot indicates the median, interquartile range and the minimum and maximum. Two-sided statistic test, $^{***}P<0.001$, $^{*}P<0.05$ Wilcoxon sum-rank test for each compared to <2 FC. **c**, Changes to Fit-Hi-C interaction signal 1 h after KA between differential ATAC-seq peaks and TSSs of AI or AD genes as detected by DESeq2 analysis. The boxplot indicates the median, interquartile range and the minimum and maximum. Two-sided statistic test, $^{*}P<0.05$ Wilcoxon rank-sum test. Sample sizes are the same as those in **b**. **d**, Top: snapshot of the *Fos* locus presenting de novo promoter–enhancer interactions in response to SE. Red arrows indicate significant activity-driven interactions 1 h after KA. Significant differences were tested for enrichment in KA-1 h samples using a one-sided confidence interval using all interaction bins in the immediate vicinity ($n=21$). Significance was assigned if the FC was above a 99.9% confidence interval giving rise to $^{*}P<0.001$. Bottom: genomic profiles at the different time points. Values are in RPM. **e**, Changes to gene loop signal (TSS–TTS) 1 h after KA for AI and AR genes detected by nuRNA-seq and DESeq2 analyses. The boxplot indicates the median, interquartile range and the minimum and maximum. Two-sided statistic test, $^{*}P<0.05$ Wilcoxon rank-sum test. Sample sizes are the same as in **b**. **f**, Metagene plot for TSS interaction signal at upregulated genes 1 h after saline or KA administration (compare with Fig. 3d). **g**, Snapshot of the *Bdnf* locus presenting the increased interaction between the TSS and the TTS. Significant differences were tested and assigned as indicated in **d** ($n=16$). **h**, Changes to the Fit-Hi-C 1 h and 48 h interaction signals between the TSSs of AI genes and DARs located at enhancers and showing increased accessibility only at 1 h (Excl 1 h) or from 1 h to 48 h (Maintained) according to our DESeq2 analysis. The boxplot indicates the median, interquartile range and the minimum and maximum. Significance was assigned using a two-sided Wilcoxon rank-sum test. Left boxplot: $n=774$, $^{*}P<0.001$. Right boxplot: $n=269$, $^{*}P=0.03$. **i**, Genomic screenshots for *Nptx2* (an example of an activity-regulated gene that does not return to basal expression and maintains some proximal chromatin accessibility changes after 48 h). The Hi-C inset for *Nptx2* shows augmented interactions with an upstream enhancer that remains slightly over the basal level even after 48 h. Red arrows indicate significant activity-driven interactions. Values show counts in RPM. Significant differences were tested and assigned as indicated in **d** ($n=81$). **j**, Schematic summarizing the main features of the immediate (top scheme) and deferred (48 h later, bottom scheme) epigenetic signature of neuronal activation; the black arrow indicates the transition over time. Enh, enhancer.

RNAPII signal (Fig. 3d), point to a continuous reloading of the RNAPII complex at IEGs during SE.

We next investigated whether these activity-induced interactions persist beyond the transcriptional burst. The Hi-C maps were consistent with ATAC-seq profiles and presented largely restored compartments (Fig. 7b, gray boxes), but incomplete restoration of site-specific interactions, 48 h after SE (Fig. 7h,i and Supplementary Fig. 10j,k; see also black lines in Fig. 7d,g). In some genes, such as *Nptx2*, which encodes a synaptic protein involved in excitatory synapse formation[42], the chromatin change was associated with enhanced transcription and strengthening of the interaction between the promoter and a proximal enhancer (Fig. 7i). Together with the identification of long-lasting changes in chromatin occupancy, these intriguing results support the notion of a genomic memory in the form of architectural modifications that originate from past transcriptional activity (Fig. 7j).

Discussion

Here we investigated the transcriptional and chromatin changes occurring in neuronal nuclei of adult behaving mice following activation. To gain cell-type specificity, we genetically tagged the nuclei and polysomes of excitatory hippocampal neurons to enable specific isolation and for use in several sequencing methods. Subsequent multi-omics analyses revealed an unexpectedly broad and dynamic

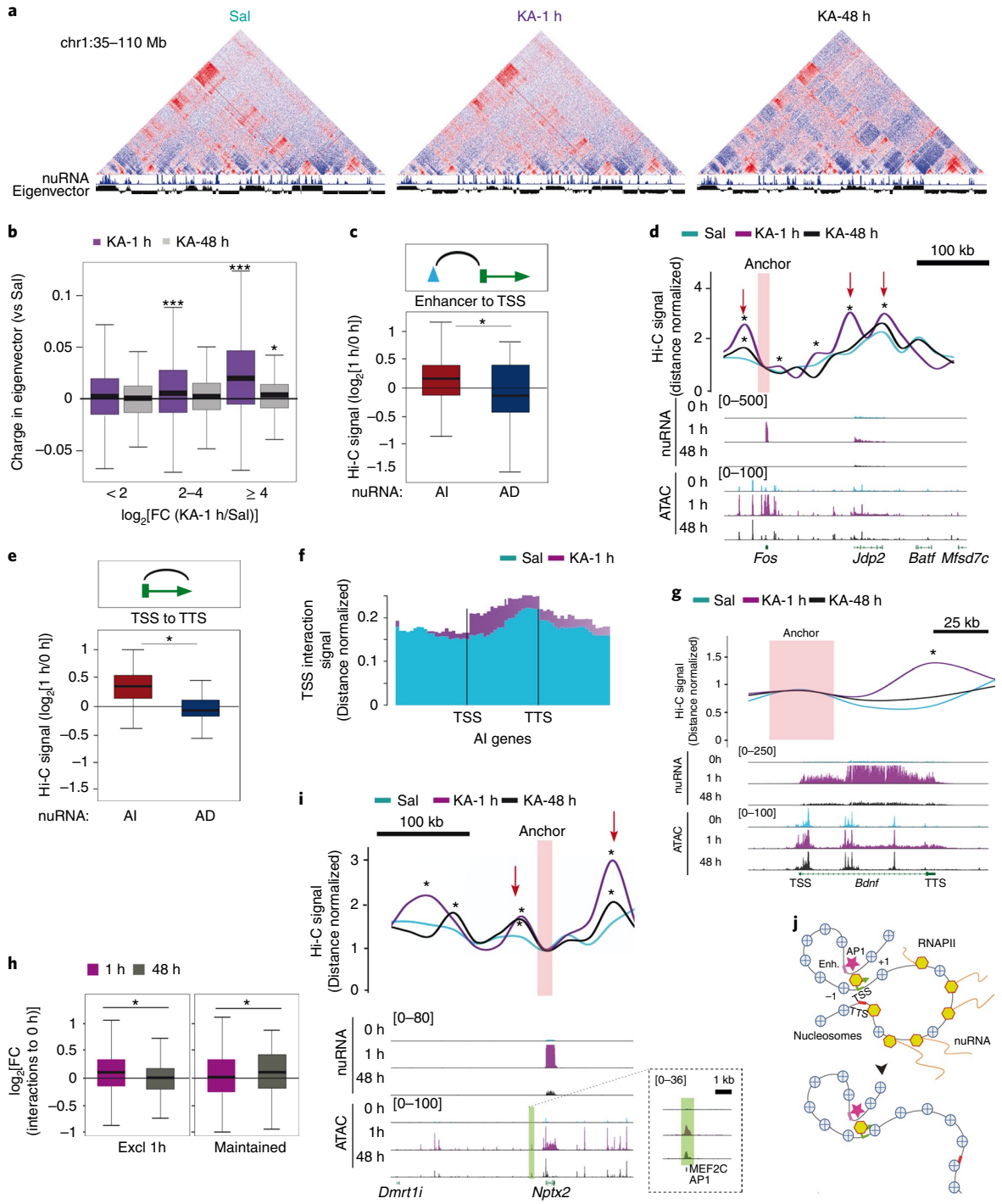

scenario, with multiple levels of activity-dependent regulation. For instance, the improved temporal resolution obtained by nuRNA profiling revealed that the robust induction of IEGs is accompanied by the downregulation of numerous metabolism genes, which suggested that the activity-induced transcriptional burst transiently hijacks the transcriptional machinery. In turn, the delayed downregulation of genes involved in ion transport and synaptic transmission may contribute to homeostatic plasticity mechanisms that compensate for prolonged activation and stabilizes neuronal firing[43]. Our nuRNA-seq screen also revealed the production of ecRNA in activity-induced genes that may fine-tune the activity of these loci and contribute to transcriptional memory[8]. Furthermore, its comparison with translatome data identified genes in which synaptic activity specifically regulates ribosome engagement. However, we cannot discard the possibility of a delayed impact at the translational level.

Further integration of nuRNA-seq with ATAC-seq, RNAPII ChIP-seq and Hi-C maps obtained in the same activation paradigm demonstrated, to our knowledge, for the first time that the robust transcription of IEGs during SE relies on the formation of gene loops that bring together the TSS and the TTS and might favor the continuous reloading of the RNAPII complex. Such organization has been described for highly transcribed genes in yeast[44,45] and *Drosophila* cells[39], but not in neurons. Our analyses also identified hundreds of de novo or strengthened promoter–enhancer interactions and thousands of TF-binding events in the chromatin of hippocampal excitatory neurons following activation. Although some of these changes are transcription-independent and rely on the post-translational modification of TFs (for example, phosphorylation), many others, such as the AP1 binding detected after both physiological and pathological stimulation, are transcription-dependent. Interestingly, the comparison of chromatin changes associated with physiological and pathological neuronal activation demonstrates that, in addition to common mechanisms, there are remarkable differences in the scope and magnitude of the changes. These large-scale and dynamic adjustments of genome topology likely contribute to the rapid and coordinated transcriptional response associated with neuronal activation in both paradigms. The technical developments introduced here in combination with recent progress in tagging neuronal ensembles that participate in the encoding of a particular experience[46] open the possibility of longitudinal studies of chromatin changes linked to memory engrams.

Notably, our longitudinal analyses in the context of SE retrieved changes in chromatin occupancy that persisted even 2 days after stimulation. In particular, changes in the occupancy of AP1-binding sites were detected long after the shutdown of the encoding loci and constituted a prominent part of the deferred epigenomic signature of neuronal activation. This conclusion is in agreement with the recent observation of stable accessibility changes in granular neurons 24 h after electrical stimulation and the postulated role of Fos in initiating neuronal activity-induced chromatin opening[26]. Intriguingly, a recent large-scale study of accessible *cis*-regulatory elements across multiple human tissues revealed that single nucleotide polymorphisms within AP1 motifs, including disease-associated noncoding variants, are often associated with changes in chromatin accessibility[1,47]. Consistent with this link, our functional genomics analyses indicated that these long-lasting changes might relate to brain disorders such as cognitive dysfunction, dementia and neurodegenerative diseases. In a broader context, the enduring changes in accessibility that are associated with de novo AP1 binding to distal regulatory regions of activity-induced genes and with enhanced promoter–enhancer interactions may influence future activities of the loci. AP1 has been recently shown to recruit the BAF chromatin–remodeling complex to enhancers to locally augment chromatin accessibility[48]. Therefore, the robust induction of AP1 subunits in response to activity might produce an excess of proteins to guarantee the occupancy of these sites and the priming effect. Since many of these loci play important roles in regulating synaptic plasticity and excitability, the experience fingerprints that persist in the chromatin may act as a form of metaplasticity by influencing the future response of the neuron to the same or other stimuli.

Online content

Any methods, additional references, Nature Research reporting summaries, source data, statements of code and data availability and associated accession codes are available at https://doi.org/10.1038/s41593-019-0476-2.

Received: 11 February 2019; Accepted: 23 July 2019;
Published online: 09 September 2019

References

1. Yap, E. L. & Greenberg, M. E. Activity-regulated transcription: bridging the gap between neural activity and behavior. *Neuron* **100**, 330–348 (2018).
2. Benito, E. & Barco, A. The neuronal activity-driven transcriptome. *Mol. Neurobiol.* **51**, 1071–1088 (2015).
3. West, A. E. & Greenberg, M. E. Neuronal activity-regulated gene transcription in synapse development and cognitive function. *Cold Spring Harb. Perspect. Biol.* **3**, a005744 (2011).
4. Eagle, A. L., Gajewski, P. A. & Robison, A. J. Role of hippocampal activity-induced transcription in memory consolidation. *Rev. Neurosci.* **27**, 559–573 (2016).
5. Sweatt, J. D. The emerging field of neuroepigenetics. *Neuron* **80**, 624–632 (2013).
6. Lopez-Atalaya, J. P. & Barco, A. Can changes in histone acetylation contribute to memory formation? *Trends Genet.* **30**, 529–539 (2014).
7. Kim, T. K. et al. Widespread transcription at neuronal activity-regulated enhancers. *Nature* **465**, 182–187 (2010).
8. Savell, K. E. et al. Extra-coding RNAs regulate neuronal DNA methylation dynamics. *Nat. Commun.* **7**, 12091 (2016).
9. You, X. et al. Neural circular RNAs are derived from synaptic genes and regulated by development and plasticity. *Nat. Neurosci.* **18**, 603–610 (2015).
10. Crepaldi, L. et al. Binding of TFIIIC to sine elements controls the relocation of activity-dependent neuronal genes to transcription factories. *PLoS Genet.* **9**, e1003699 (2013).
11. Madabhushi, R. et al. Activity-induced DNA breaks govern the expression of neuronal early-response genes. *Cell* **161**, 1592–1605 (2015).
12. Cho, J. et al. Multiple repressive mechanisms in the hippocampus during memory formation. *Science* **350**, 82–87 (2015).
13. Mauger, O., Lemoine, F. & Scheiffele, P. Targeted intron retention and excision for rapid gene regulation in response to neuronal activity. *Neuron* **92**, 1266–1278 (2016).
14. Mo, A. et al. Epigenomic signatures of neuronal diversity in the mammalian brain. *Neuron* **86**, 1369–1384 (2015).
15. Ben-Ari, Y. & Cossart, R. Kainate, a double agent that generates seizures: two decades of progress. *Trends Neurosci.* **23**, 580–587 (2000).
16. Elliott, R. C., Miles, M. F. & Lowenstein, D. H. Overlapping microarray profiles of dentate gyrus gene expression during development- and epilepsy-associated neurogenesis and axon outgrowth. *J. Neurosci.* **23**, 2218–2227 (2003).
17. Huang, Y., Doherty, J. J. & Dingledine, R. Altered histone acetylation at glutamate receptor 2 and brain-derived neurotrophic factor genes is an early event triggered by status epilepticus. *J. Neurosci.* **22**, 8422–8428 (2002).
18. Tsankova, N. M., Kumar, A. & Nestler, E. J. Histone modifications at gene promoter regions in rat hippocampus after acute and chronic electroconvulsive seizures. *J. Neurosci.* **24**, 5603–5610 (2004).
19. Crosio, C., Heitz, E., Allis, C. D., Borrelli, E. & Sassone-Corsi, P. Chromatin remodeling and neuronal response: multiple signaling pathways induce specific histone H3 modifications and early gene expression in hippocampal neurons. *J. Cell Sci.* **116**, 4905–4914 (2003).
20. Taniura, H., Sng, J. C. & Yoneda, Y. Histone modifications in status epilepticus induced by kainate. *Histol. Histopathol.* **21**, 785–791 (2006).
21. Dougherty, J. D. The expanding toolkit of translating ribosome affinity purification. *J. Neurosci.* **37**, 12079–12087 (2017).
22. Schott, J. et al. Translational regulation of specific mRNAs controls feedback inhibition and survival during macrophage activation. *PLoS Genet.* **10**, e1004368 (2014).
23. Yamazaki, S., Muta, T., Matsuo, S. & Takeshige, K. Stimulus-specific induction of a novel nuclear factor-κB regulator, IκB-ζ, via Toll/interleukin-1 receptor is mediated by mRNA stabilization. *J. Biol. Chem.* **280**, 1678–1687 (2005).

24. Behrens, G. et al. A translational silencing function of MCPIP1/regnase-1 specified by the target site context. *Nucleic Acids Res.* **46**, 4256–4270 (2018).
25. Buenrostro, J. D., Giresi, P. G., Zaba, L. C., Chang, H. Y. & Greenleaf, W. J. Transposition of native chromatin for fast and sensitive epigenomic profiling of open chromatin, DNA-binding proteins and nucleosome position. *Nat. Methods* **10**, 1213–1218 (2013).
26. Su, Y. et al. Neuronal activity modifies the chromatin accessibility landscape in the adult brain. *Nat. Neurosci.* **20**, 476–483 (2017).
27. Wang, S. et al. Target analysis by integration of transcriptome and ChIP-seq data with BETA. *Nat. Protoc.* **8**, 2502–2515 (2013).
28. Saha, R. N. et al. Rapid activity-induced transcription of Arc and other IEGs relies on poised RNA polymerase II. *Nat. Neurosci.* **14**, 848–856 (2011).
29. Schep, A. N. et al. Structured nucleosome fingerprints enable high-resolution mapping of chromatin architecture within regulatory regions. *Genome Res.* **25**, 1757–1770 (2015).
30. Wang, Y., Lu, J. J., He, L. & Yu, Q. Triptolide (TPL) inhibits global transcription by inducing proteasome-dependent degradation of RNA polymerase II (Pol II). *PLoS One* **6**, e23993 (2011).
31. Jonkers, I., Kwak, H. & Lis, J. T. Genome-wide dynamics of Pol II elongation and its interplay with promoter proximal pausing, chromatin, and exons. *eLife* **3**, e02407 (2014).
32. Creyghton, M. P. et al. Histone H3K27ac separates active from poised enhancers and predicts developmental state. *Proc. Natl Acad. Sci. USA* **107**, 21931–21936 (2010).
33. Malik, A. N. et al. Genome-wide identification and characterization of functional neuronal activity–dependent enhancers. *Nat. Neurosci.* **17**, 1330–1339 (2014).
34. Hardingham, G. E., Pruunsild, P., Greenberg, M. E. & Bading, H. Lineage divergence of activity-driven transcription and evolution of cognitive ability. *Nat. Rev. Neurosci.* **19**, 9–15 (2018).
35. Guzowski, J. F. et al. Mapping behaviorally relevant neural circuits with immediate-early gene expression. *Curr. Opin. Neurobiol.* **15**, 599–606 (2005).
36. Lacar, B. et al. Nuclear RNA-seq of single neurons reveals molecular signatures of activation. *Nat. Commun.* **7**, 11022 (2016).
37. Tai, X. Y. et al. Hyperphosphorylated tau in patients with refractory epilepsy correlates with cognitive decline: a study of temporal lobe resections. *Brain* **139**, 2441–2455 (2016).
38. Halder, R. et al. DNA methylation changes in plasticity genes accompany the formation and maintenance of memory. *Nat. Neurosci.* **19**, 102–110 (2016).
39. Rowley, M. J. & Corces, V. G. Organizational principles of 3D genome architecture. *Nat. Rev. Genet.* **19**, 789–800 (2018).
40. Bonev, B. et al. Multiscale 3D genome rewiring during mouse neural development. *Cell* **171**, 557–572.e524 (2017).
41. Rao, S. S. et al. A 3D map of the human genome at kilobase resolution reveals principles of chromatin looping. *Cell* **159**, 1665–1680 (2014).
42. Xiao, M. F. et al. NPTX2 and cognitive dysfunction in Alzheimer's disease. *eLife* **6**, e23798 (2017).
43. Fernandes, D. & Carvalho, A. L. Mechanisms of homeostatic plasticity in the excitatory synapse. *J. Neurochem.* **139**, 973–996 (2016).
44. Hampsey, M., Singh, B. N., Ansari, A., Laine, J. P. & Krishnamurthy, S. Control of eukaryotic gene expression: gene loops and transcriptional memory. *Adv. Enzym. Regul.* **51**, 118–125 (2011).
45. Laine, J. P., Singh, B. N., Krishnamurthy, S. & Hampsey, M. A physiological role for gene loops in yeast. *Genes Dev.* **23**, 2604–2609 (2009).
46. DeNardo, L. & Luo, L. Genetic strategies to access activated neurons. *Curr. Opin. Neurobiol.* **45**, 121–129 (2017).
47. Maurano, M. T. et al. Large-scale identification of sequence variants influencing human transcription factor occupancy in vivo. *Nat. Genet.* **47**, 1393–1401 (2015).
48. Vierbuchen, T. et al. AP-1 transcription factors and the BAF complex mediate signal-dependent enhancer selection. *Mol. Cell* **68**, 1067–1082.e1012 (2017).
49. Del Blanco, B. et al. CBP and SRF co-regulate dendritic growth and synaptic maturation. *Cell Death Differ*. https://doi.org/10.1038/s41418-019-0285-x (2019).
50. Scandaglia, M. et al. Loss of Kdm5c causes spurious transcription and prevents the fine-tuning of activity-regulated enhancers in neurons. *Cell Rep.* **21**, 47–59 (2017).

Acknowledgements

The authors thank E. Herrera, T. Ferrar, J. P. Lopez-Atalaya and Y. Ruan for their critical reading of the manuscript, and R. Olivares, N. Cascales, A. Caler and the personnel of the sequencing facility at the CRG (Barcelona, Spain) and HudsonAlpha (Alabama, USA) for technical assistance. J.F.-A. and M.T.L.-C. are recipients of fellowships from the Spanish Ministry of Science and Innovation (MICINN, SVP-2014-068387 and BES-2017-081298, respectively). The research of A.B. is supported by grants SAF2017-87928-R and SEV-2017-0723 from the MICINN co-financed by the ERDF, PROMETEO/2016/026 from the Generalitat Valenciana and RGP0039/2017 from the Human Frontiers Science Program Organization (HFSPO). M.J.R. is supported by the National Institutes of Health (NIH) Pathway to Independence Award K99/R00 GM127671. The research of V.G.C. is supported by the US Public Health Service Award (R01) GM035463 from the NIH. The content of the article is solely the responsibility of the authors and does not necessarily represent the official views of the NIH. The Instituto de Neurociencias is a "Centre of Excellence Severo Ochoa".

Author contributions

J.F.-A. performed most of the experiments and bioinformatic analyses. M.L. collaborated in the characterization of the models and performed ChIP-seq experiments. M.T.L.-C. collaborated in the bioinformatic analyses and preparation of the figures. M.J.R. conducted the Hi-C analyses. A.M.M.-G. collaborated in the preparation of Hi-C samples and performed some of the immunostaining analyses. B.d.B. provided important reagents. V.G.C. supervised the Hi-C experiments and analyses. A.B. supervised all other aspects of the project. A.B. and J.F.-A. conceived the study, designed the experiment and wrote the original draft. All the authors discussed the findings and revised the final version of the manuscript.

Competing interests

The authors declare no competing interests.

Additional information

Supplementary information is available for this paper at https://doi.org/10.1038/s41593-019-0476-2.

Reprints and permissions information is available at www.nature.com/reprints.

Correspondence and requests for materials should be addressed to A.B.

Peer review information: *Nature Neuroscience* thanks Schahram Akbarian, Michael Greenberg, and the other, anonymous, reviewer(s) for their contribution to the peer review of this work.

Methods

Animals and treatments. The generation of CaMKIIα-creERT2 (ref. [51]) (from the European Mouse Mutant Archive *EMMA* strain 02125), the cre-dependent riboTRAP[52] (Jackson Laboratory, stock no. 030305) and SUN1-tagged mice[14] (Jackson Laboratory, stock no. 021039) have been previously described. Mice were maintained and bred under standard conditions, consistent with Spanish and European regulations and approved by the Institutional Animal Care and Use Committee. All strains where maintained in a pure C57BL/6J background. Experiments were conducted using 3–6-month-old male animals. Mice received intragastric administration of tamoxifen as previously described[53] when they were ~2 months old, and we waited 3–4 weeks before experimentation. For the induction of SE by KA (Milestone PharmTech USA), a concentration of 25 mg per kg was intraperitoneally injected. For the blocking of transcription by TPL (from *Tripterygium wilfordii*, Abcam ab120720) a concentration of 0.8 mg per kg was intraperitoneally injected per mice 2 h before the injection of KA or saline.

Behavioral tasks. For NE, individually housed mice received 3–4 days of 5 min of handling before exposing them to a novel environment. The arena consisted of a white acrylic box (48 × 48 × 30 cm) containing objects with different forms and colors. A total of six mice were individually placed for 60 min in the arena. The mice were then processed for microdissection of the hippocampus and for FANS. The novel object location memory test followed a previously described protocol[54]. Briefly, 1 week after saline or KA administration, a total of eight to nine mice per condition were individually habituated to an empty arena (two exposures of 5 min each on consecutive days). For training, the same mice were placed for 10 min in the arena with two identical objects 24 h after the last habituation session. For location memory testing 24 h after training, one of the two objects was moved to a new location. The time spent exploring each object was quantified, and a differential index (DI) was calculated as follows: DI = time exploring the displaced object – time exploring the non-displaced object/total time exploring both objects.

Immunohistochemistry and microscopy. Mice were anesthetized with an intraperitoneal injection of ketamine/xylazine, perfused with 4% paraformaldehyde in PBS and extracted brains were postfixed overnight at 4 °C. Coronal or sagittal vibratome 40-µm sections were obtained, washed in PBS and PBS–0.1% Triton X-100 (PBT). Sections were incubated for 30 min with blocking buffer 5% newborn calf serum (NCS, Sigma N4762) and PBT, and incubated overnight at 4 °C with the primary antibodies diluted in 5% NCS-PBT. The following primary antibodies were used in this study: α-NeuN (1:2,000; Chemicon, MAB377), α-GAD67 (1:800; Millipore, MAB5406), α-Fos (1:500; Synaptic Systems, 226004) and α-GFP (1:1,000; Aves Labs, GFP-1020). After primary antibody incubation and washing with PBS, sections were incubated with a guinea pig IgG (H+L) Alexa 594 (1:400; Invitrogen, A-11075) for fluorescent labeling. Nuclei were counterstained with 1 nM of 4,6-diamidino-2-phenylindole (DAPI) solution (Invitrogen) before mounting with Fluoromount (Sigma). Images were taken using an Olympus confocal inverted microscope and processed using ImageJ.

Ribosomal RNA immunoprecipitation sequencing. TRAP immunoprecipitation followed the original protocol as previously described[55], but with small changes to the extraction step. Hippocampi were microdissected after cervical dislocation, washed in PBS and submerged in ribosomal extraction buffer (REB-LOW: 150 mM KCl, 10 mM $MgCl_2$, 20 mM HEPES-KOH (pH 7.8), 1% IGEPAL CA-630, 0.5 mM β-mercaptoethanol, 1× proteinase inhibitors (cOmplete EDTA-free, Roche), 60 U ml^{-1} RNasin Plus RNasa (Promega N2611), 100 µg ml^{-1} cycloheximide). Tissue was homogenized (25 times with pestle A and B) using a dounce homogenizer (K8853000002, Kontes-DWK). A total of six hippocampi were pooled together and nuclear supernatant was obtained by centrifugation at 2,000 × *g* at 4 °C for 10 min. The subsequent steps followed the original protocol.

FANS. A novel protocol was designed for maximum efficiency and specificity, and to obtain a total of 1 million nuclei per mice. Hippocampi were microdissected after cervical dislocation, rapidly washed in PBS and extracted using a dounce homogenizer (Sigma) with 1 ml of nuclear extraction buffer (NEB: 250 mM sucrose, 25 mM KCl, 5 mM $MgCl_2$, 20 mM HEPES-KOH (pH 7.8), 0.5% IGEPAL CA-630, 65 mM β-glycerol, 1 mM β-mercaptoethanol, 1× proteinase inhibitors (cOmplete EDTA-free, Roche), 0.2 mM spermine, 0.5 mM spermidine, 60 U ml^{-1} RNasin Plus RNasa (Promega, N2611), 5% NCS). Tissue was disrupted 15 times with pestle A and B, as described above. For nuclei fixation, formaldehyde was added at a final concentration of 1% after extraction, incubated at room temperature on a rotator for 10 min, and then blocked with 1.25 mM glycine. Hippocampi from three (SE experiments) to six (NE experiment) mice were pooled and then filtered through a 35-µm mesh capped tube. For nuclear staining, the nuclei pool was split into two tubes of 750 µl total NEB and were stained for 30 min with the primary antibody α-Fos-Alexa647 (1:40; sc-52, AF647) or α-NeuN (1:100; Chemicon, MAB377) at 4 °C on a rotator. For α-NeuN, the secondary antibody Alexa Fluor-conjugated IgG (1:1,000; Life Technologies) was incubated for another 15 min at 4 °C on a rotator. Nuclei were stained for 10 min with DAPI (at a final concentration of 0.01 mM). After incubation, the nuclei preparation was diluted in Optiprep density gradient medium (60% iodixanol, Sigma D1556) up to a concentration of 22%. A density gradient was prepared in a 13-ml ultracentrifuge tube containing 44% Optiprep at the bottom layer and 22% Optiprep in the upper layer for nuclear extraction. The tube was centrifuged at 7,500 r.p.m. for 23 min at 4 °C, and the nuclear fraction was collected and transferred into a tube with the same volume of nuclear isolation buffer (NIB: 340 mM sucrose, 25 mM KCl, 5 mM $MgCl_2$, 20 mM HEPES-KOH (pH 7.8), 65 mM β-glycerol, 1× proteinase inhibitors (cOmplete EDTA-free, Roche), 0.2 mM spermine, 0.5 mM spermidine, 60 U ml^{-1} RNasin Plus RNase (Promega, N2611), 5% NCS). Nuclei populations were selected using a FACS Aria III (BD Biosciences) for DAPI staining, singlet nuclei, SUN1-GFP^+ positive staining, and sorted into a tube containing NIB. Flow cytometry data were analyzed and plotted using FlowJo (v.10).

Quantitative PCR with reverse transcription and RNA library construction. Bulk RNA extraction from dissected hippocampi was done using TRI reagent (Sigma-Aldrich). For TRAP-isolated RNA, after overnight incubation, beads were washed three to four times in ribosomal extraction buffer (RIB-HIGH: 350 mM KCl, 10 mM $MgCl_2$, 20 mM HEPES-KOH (pH 7.8), 1% IGEPAL CA-630, 0.5 mM β-mercaptoethanol) and resuspended in 350 µl of RLT buffer for purification using a RNeasy Micro kit (Qiagen, 74004). For nuclear RNA, after FANS, 2 million nuclei were pelleted at 4 °C, 1,000 × *g* for 7 min and resuspended in RLT buffer for purification using the RNeasy Micro kit. Quantitative PCR (qPCR) was performed using an Applied Biosystems 7300 real-time PCR unit. RNA samples were reverse transcribed using a RevertAid First-Strand cDNA synthesis kit (Fermentas) and quantified using Eva Green qPCR reagent mix. Samples were assayed in duplicate and the results were normalized to *Gapdh* transcript levels. The following primer sequences were used in the qPCR with reverse transcription (RT–qPCR) assays:

Fos Forward	5′-GCTTCCCAGAGGAGATGTCTGT
Fos Reverse	5′-GCAGACCTCCAGTCAAATCCA
Npas4 Forward	5′-CTGGCCCAAGCTTCTTCTCA
Npas4 Reverse	5′-TCCATGCTTGGCTTGAAGTCT
Arc Forward	5′-GCAGGAGAACTGCCTGAACAG
Arc Reverse	5′-AAGACTGATATTGCTGAGCCTCAA
Plp1 Forward	5′-CTTTGGCGACTACAAGACCAC
Plp1 Reverse	5′-ACAGTCAGGGCATAGGTGATG
Gfap Forward	5′-GGACAACTTTGCACAGGACCTC
Gfap Reverse	5′-TCCAAATCCACACGAGCCA
Bdnf Forward	5′-GAAGGTTCGGCCCAACGA
Bdnf Reverse	5′-CCAGCAGAAAGAGTAGAGGAGGC
Gapdh Forward	5′-CATGGACTGTGGTCATGAGCC
Gapdh Reverse	5′-CTTCACCACCATGGAGAAGGC

RNA-seq, library preparation and sequencing were performed at facilities in the Center for Genomic Regulation (CRG, Barcelona, Spain). Truseq libraries were prepared from ribo-depleted total RNA for nuRNA-seq and from polyA-selected mRNA in the case of riboRNA-seq. Samples were sequenced (single-end, 50 base pairs in length) using an Illumina HiSeq2500 apparatus with a depth of at least 80 million reads for nuRNA and 30 million reads for riboRNA (Supplementary Table 8a).

ATAC assay and ATAC-seq library construction. After FANS, 50,000 nuclei were pelleted at 4 °C, 1,000 × *g* for 7 min, resuspended in 50 µl of transposition reaction (Illumina, FC-121-1030) and gently pipetted to resuspend the nuclei. The ATAC-seq experiments were conducted as previously described [25]. Briefly, nuclei were incubated with Tn5 for 30 min at 37 °C and then immediately purified using a MinElute PCR purification kit (Qiagen, 28004). To reduce PCR-induced biases during library preparation, after the first 5 PCR cycles, 10% of the sample was monitored with SYBR-green qPCR for 20 cycles to calculate the 25% of saturation per sample (every sample needed more than 12 PCR cycles in total). Libraries were purified using the MinElute PCR purification kit. ATAC assays were performed in an Applied Biosystems 7300 real-time PCR unit using Eva Green qPCR reagent mix. Samples were assayed in duplicate, and results were normalized to *Gapdh* promoter insertion levels. The following sequences of primer pairs were used in the ATAC–qPCR assays:

Heterochromatin Forward	5′-CTACCGAGTGTTGATTGCCGT
Heterochromatin Reverse	5′-TGATGCAAGTGTCAAGCTCAATG
Fos-promoter Forward	5′-GCAGTCGCGGTTGGAGTAGT
Fos-promoter Reverse	5′-CGCCCAGTGACGTAGGAAGT
Gfap-promoter Forward	5′-TACCAGAAAGGGGGTTCCTT
Gfap-promoter Reverse	5′-AACTCCTCTCACCCCACTGA
Gapdh-promoter Forward	5′-TTCACCTGGCACTGCACAA
Gapdh-promoter Reverse	5′-CCACCATCCGGGTTCCTATAA

For ATAC-seq, sequencing (paired-end, 50 bp in length) was performed at the CRG facilities using an Illumina HiSeq2500 apparatus and a depth of at least 100 million reads per sample (Supplementary Table 8a).

ChIP assay and ChIP library construction. For bulk ChIP, the whole hippocampi from two mice were microdissected and pooled together. For sorted ChIP after FANS, 2 million nuclei were pelleted at 4 °C, 2,000 × *g* for 7 min and re-suspended in SDS lysis buffer or RIPA-PBS buffer. ChIP was conducted as previously described[56] using anti-H3K4me3 (Millipore, 07-473), anti-H3K27ac (Abcam, ab4729), anti-CBP (sc583x) and anti-RNAPII (sc901x) antibodies. ChIP assays were performed in an Applied Biosystems 7300 real-time PCR unit using Eva Green qPCR reagent mix. Samples were assayed in duplicate, and results were normalized to input. The following sequences of primer pairs were used in the ChIP–qPCR assays:

Camk2a-promoter Forward	5′-GAGTCCTAGAGAGCATGGGG
Camk2a-promoter Reverse	5′-TGCATACACAGTGCTTCCAAA
Heterochromatin Forward	5′-CTACCGAGTGTTGATTGCCGT
Heterochromatin Reverse	5′-TGATGCAAGTGTCAAGCTCAATG

For ChIP-seq, library preparation and sequencing (single-end, 50 bp in length) were performed at the CRG facilities in a Illumina Hi2500Seq apparatus with a depth of 40 million reads per sample (Supplementary Table 8a).

In situ Hi-C library construction. After FANS, 2 million nuclei were pelleted at 4 °C, 2,000 × *g* for 10 min. The nuclei were resuspended in ice-cold Hi-C lysis buffer, and the original in situ Hi-C protocol was followed as previously described[41]. Libraries were prepared with TruSeq primers and sequenced (paired-end 50 bp) in an Illumina NovaSeq apparatus at the Hudson Alpha sequencing facility (Alabama, AL, USA) with a depth of 1 billion reads per sample (Supplementary Table 8a).

Genomic data processing and access. All sequenced dataset adapters were trimmed using cutadapt (v.1.18)[57] and aligned to mm10. Only reads with mapq >30 and mapping to nuclear chromosomes were used for further analysis. Data were processed with the extensive use of custom scripts and Samtools (v.1.9)[58], bedtools (v.2.26.0)[59] and DeepTools (v.3.1.0)[60]. Whole genome alignments were normalized to RPM (read per million sequenced reads) and visualized using IGV (v.2.3.92)[61]. The datasets generated in this study are listed in Supplementary Table 8a and can be accessed at the GEO repository using the accession number GSE125068. The previously generated datasets deposited in public servers used in specific analyses are listed in Supplementary Table 8b.

RNA-seq data. Reads were aligned using HISAT2 (v.2.1.0)[62]. For a clear comparison between riboRNA and nuRNA datasets, reads were annotated to exons from Ensemble (GRCm38.89) and quantified using Rsubreads (v.1.26)[63]. Differential expression analysis was performed in DESeq2 (v.1.10.0)[64], accounting for batch and treatment effect. Genes with false discovery rate (FDR) values of <0.1 and $\log_2$ fold change (FC) values of >+/−1 were considered significantly changed. Transcriptome analyses used the datasets GSE74971 (ref. [38]) and GSE77067 (ref. [36]), applying the same cut-offs used in our study. Comparison of principal neurons (this study) to cortical neurons and embryonic stem cells from GSE96107 (ref. [40]) was done using fragments per kilobase of transcript per million mapped read values from each dataset. GO terms where analyzed using Panther (v.14) with Fisher's exact tests and FDR multiple test correction. Cut-off was based on the number of genes associated to the category (<2,000 genes), the number of DEG associated to the category (>3 genes) and fold enrichment >3 ($P < 0.05$). Over-representation enrichment analysis was performed using WebGestalt, and the use of the DisGeNET human database[65,66].

ATAC-seq data. Reads were aligned using bowtie2 (v.2.2.6)[67]. Duplicated reads were removed using Picardtools (v.2.17) and only paired reads were used for further analysis (the KA-6 h biological replicate 1 had to be down-sampled). The same pipeline was applied to ATAC-seq datasets from GSE63137 (ref. [14]) and GSE82015 (ref. [26]). Peak calling was done using MACS2 (ref. [68]) in the merged samples that were used to compare DARs, quantified using Rsubreads on called peaks with FDR < 1×10^{-5}. For differential accessible genes (DAGs), reads were annotated to the whole gene region from Ensembl (GRCm38.89) and quantified using Rsubreads (v.1.26)[63]. DAR and DAG analyses were performed using DESeq2 (v.1.10.0)[64], accounting for batch and treatment effect. Regions or genes with FDR < 0.1 and $\log_2$(FC) >+/−1 were considered significantly changed. The analysis of changes in TPL and NE experiments were performed using DESeq2, including the comparisons with KA-1 h and saline samples, respectively, that support the reduced *n* for the rlog calculation and value transformations. Unfortunately, due to the broad increase of accessibility at gene bodies, we could not subtract polymerase-driven transcriptional events from putative enhancers located at introns; the enhancer regions considered in this study were those positioned a more than 1 kb from the TSS (upstream) or TTS (downstream) of annotated Ensembl genes (GRCm38.89). GO term enrichments for DAGs were analyzed using Panther with Fisher's exact test and FDR multiple test correction. Cut-off was based on the number of genes associated to the category (<2,000 genes), the number of DEGs associated to the category (>3 genes) and fold enrichment >3 ($P < 0.05$). Disease ontology from genes associated to DARs was done using GREAT (v.3.0)[69] using standard parameters. Promoter and enhancer regions were clustered using an unsupervised method (*k*-means with linear normalization method) using seqMiner (v.1.3.4)[70]. The phastCons score was obtained from the multiple alignments of 59 vertebrate genomes (60way Placental) to the mouse genome mm10 (refs. [71,72]). Motif analysis was done at the promoter and enhancer sites using HOMER (v.4.8). Motifs were classified by families (that is, the TRE motif is recognized by a number of proteins that form the AP1 complex) and by the detection of the related protein-coding genes in our nuRNA-seq datasets. Predictive analysis of DARs and expression changes were done using BETA (v.1.0.7), with the basic activating/repressive function prediction with the Ensembl reference (GRCm38.89) and DEG from our nuRNA-seq datasets. Nucleosome occupancy information was retrieved using the NucleoATAC algorithm (v.0.3.4)[29]; the shifting analysis was conducted using custom R scripts. Digital footprint analysis was done in DAR promoters and enhancers using the adapted Wellington algorithm for Tn5 (ref. [73]). ATAC-seq datasets from KA-1 h were used to detect the footprints during SE (FDR < 0.01) and in the longitudinal analysis ($P < 1 \times 10^{-10}$).

ChIP-seq data. Reads were aligned using bowtie2 (v.2.2.6)[67]. Chip-seq meta-analyses used data generated from previous studies[7,33,38,50]; in some cases the positions had to be trans-mapped to mm10. Peak calling was done using MACS2 (v.2.1.1)[68] with default parameters.

Hi-C data. Hi-C datasets were processed using the Juicer pipeline[74] to align reads to the mm10 genome, filter duplicates, perform matrix normalizations and obtain the eigenvector. Reads with a mapping quality ≥30 and binned at 25 kb were used in all downstream analyses. Distance normalization was done using the formula $\frac{(\text{Observed}-\text{expected})}{(\text{Expected}+1)}$. Significant enhancer–promoter interactions were called using Fit-Hi-C (v.1.1.3)[75] separately for each dataset with an FDR of 0.05. Fit-Hi-C interactions were compared across samples using the distance normalized signal. Intragenic interactions were visualized across genes with high and low nuRNA-seq signals categorized by the top and bottom quartiles, respectively. High-intensity interactions known as CTCF loops were identified via HiCCUPS (v.1.7.6)[41] in each dataset, and differential loops were searched for by selecting for twofold changes in interaction signals in a combined total list of loops. To examine the most dramatically changed loops in the published Hi-C data for in vitro differentiated cortical neurons and embryonic stem cells (GSE96107)[40], we searched for fourfold changes and then plotted the average distance normalized Hi-C signal in each dataset. One-dimensional interaction plots were derived by isolating all Hi-C interaction signals with each specified anchor. Because *Nptx2* lays at the border of two 25-kb bins, the average interaction signal across both bins was used.

Statistical analyses. Sets of mice with the same age and sex were raised in the same conditions and randomly allocated to the different experimental groups. Blinding was not applied in the study because the animals needed to be controlled by treatment conditions. No statistical methods were used to predetermine sample sizes, but our sample sizes were similar to those reported in similar publications[14]. In addition, sample sizes were estimated according to data variance and the correlation between biological replicates and the distance to the control condition. No data were excluded from analyses. All statistical analyses were two-tailed. For pairwise comparison of averages, data were tested for normality using Shapiro's test. If any of the two samples were significantly non-normal, a nonparametric Mann–Whitney U/Wilcoxon rank-sum test was executed instead. When variances between groups were the same, a two-way analysis of variance was applied in the riboRNA and qPCR experiments. For multiple comparisons, the Kruskal–Wallis test was applied or the Dunn test was used when the number of observations were unequal between groups. Bonferroni-corrected pairwise tests were used where appropriate post hoc to correct for multiple comparisons. *P* values were considered to be significant when $\alpha < 0.05$. Assuming the linear relation of the data, correlation was used. For bar plots and cumulative plots, centered regions indicate the mean ± s.e.m. unless otherwise indicated. Heatmaps show Euclidean clusters. For one-dimensional interaction plots, changes in interactions were significant if above the 99.9% confidence interval derived from all the FCs in the plot.

Reporting Summary. Further information on research design is available in the Nature Research Reporting Summary linked to this article.

Data availability

Supplementary Tables 1–7 provide direct access to the main results derived from the transcriptome and epigenome screens presented in this study. In addition, raw and processed datasets generated during the study are available in the GEO repository using the accession number GSE125068.

References

51. Erdmann, G., Schutz, G. & Berger, S. Inducible gene inactivation in neurons of the adult mouse forebrain. *BMC Neurosci.* **8**, 63 (2007).

52. Stanley, S. et al. Profiling of glucose-sensing neurons reveals that GHRH neurons are Activated by hypoglycemia. *Cell Metab.* **18**, 596–607 (2013).
53. Fiorenza, A. et al. Blocking miRNA Biogenesis in adult forebrain neurons enhances seizure susceptibility, fear memory, and food intake by increasing neuronal responsiveness. *Cereb. Cortex* **26**, 1619–1633 (2016).
54. Vogel-Ciernia, A. et al. The neuron-specific chromatin regulatory subunit BAF53b is necessary for synaptic plasticity and memory. *Nat. Neurosci.* **16**, 552–561 (2013).
55. Heiman, M., Kulicke, R., Fenster, R. J., Greengard, P. & Heintz, N. Cell type-specific mRNA purification by translating ribosome affinity purification (TRAP). *Nat. Protoc.* **9**, 1282–1291 (2014).
56. Lopez-Atalaya, J. P., Ito, S., Valor, L. M., Benito, E. & Barco, A. Genomic targets, and histone acetylation and gene expression profiling of neural HDAC inhibition. *Nucleic Acids Res.* **41**, 8072–8084 (2013).
57. Martin, M. Cutadapt removes adapter sequences from high-throughput sequencing reads. *EMBnet J.* **17**, 10–12 (2011).
58. Li, H. et al. The Sequence Alignment/Map format and SAMtools. *Bioinformatics* **25**, 2078–2079 (2009).
59. Quinlan, A. R., & Hall, I. M. BEDTools: a flexible suite of utilities for comparing genomic features. *Bioinformatics* **26**, 841–842 (2010).
60. Ramirez, F. et al. deepTools2: a next generation web server for deep-sequencing data analysis. *Nucleic Acids Res.* **44**, W160–W165 (2016).
61. Thorvaldsdottir, H., Robinson, J. T. & Mesirov, J. P. Integrative Genomics Viewer (IGV): high-performance genomics data visualization and exploration. *Brief. Bioinform.* **14**, 178–192 (2013).
62. Kim, D., Langmead, B. & Salzberg, S. L. HISAT: a fast spliced aligner with low memory requirements. *Nat. Methods* **12**, 357–360 (2015).
63. Liao, Y., Smyth, G. K. & Shi, W. featureCounts: an efficient general purpose program for assigning sequence reads to genomic features. *Bioinformatics* **30**, 923–930 (2014).
64. Love, M. I., Huber, W. & Anders, S. Moderated estimation of fold change and dispersion for RNA-seq data with DESeq2. *Genome Biol.* **15**, 550 (2014).
65. Bauer-Mehren, A., Rautschka, M., Sanz, F. & Furlong, L. I. DisGeNET: a Cytoscape plugin to visualize, integrate, search and analyze gene-disease networks. *Bioinformatics* **26**, 2924–2926 (2010).
66. Queralt-Rosinach, N., Pinero, J., Bravo, A., Sanz, F. & Furlong, L. I. DisGeNET-RDF: harnessing the innovative power of the Semantic Web to explore the genetic basis of diseases. *Bioinformatics* **32**, 2236–2238 (2016).
67. Langmead, B. & Salzberg, S. L. Fast gapped-read alignment with Bowtie 2. *Nat. Methods* **9**, 357–359 (2012).
68. Zhang, Y. et al. Model-based analysis of ChIP-Seq (MACS). *Genome Biol.* **9**, R137 (2008).
69. McLean, C. Y. et al. GREAT improves functional interpretation of *cis*-regulatory regions. *Nat. Biotechnol.* **28**, 495–501 (2010).
70. Ye, T. et al. seqMINER: an integrated ChIP-seq data interpretation platform. *Nucleic Acids Res.* **39**, e35 (2011).
71. Siepel, A. et al. Evolutionarily conserved elements in vertebrate, insect, worm, and yeast genomes. *Genome Res.* **15**, 1034–1050 (2005).
72. Pollard, K. S., Hubisz, M. J., Rosenbloom, K. R. & Siepel, A. Detection of nonneutral substitution rates on mammalian phylogenies. *Genome Res.* **20**, 110–121 (2010).
73. Piper, J. et al. Wellington: a novel method for the accurate identification of digital genomic footprints from DNase-seq data. *Nucleic Acids Res.* **41**, e201 (2013).
74. Durand, N. C. et al. Juicer provides a one-click system for analyzing loop-resolution hi-C experiments. *Cell Syst.* **3**, 95–98 (2016).
75. Ay, F., Bailey, T. L. & Noble, W. S. Statistical confidence estimation for Hi-C data reveals regulatory chromatin contacts. *Genome Res.* **24**, 999–1011 (2014).

nature research

Corresponding author(s): Angel Barco

Last updated by author(s): Jul 19, 2019

Reporting Summary

Nature Research wishes to improve the reproducibility of the work that we publish. This form provides structure for consistency and transparency in reporting. For further information on Nature Research policies, see Authors & Referees and the Editorial Policy Checklist.

Statistics

For all statistical analyses, confirm that the following items are present in the figure legend, table legend, main text, or Methods section.

n/a	Confirmed	
☐	☒	The exact sample size (*n*) for each experimental group/condition, given as a discrete number and unit of measurement
☐	☒	A statement on whether measurements were taken from distinct samples or whether the same sample was measured repeatedly
☐	☒	The statistical test(s) used AND whether they are one- or two-sided *Only common tests should be described solely by name; describe more complex techniques in the Methods section.*
☐	☒	A description of all covariates tested
☐	☒	A description of any assumptions or corrections, such as tests of normality and adjustment for multiple comparisons
☐	☒	A full description of the statistical parameters including central tendency (e.g. means) or other basic estimates (e.g. regression coefficient) AND variation (e.g. standard deviation) or associated estimates of uncertainty (e.g. confidence intervals)
☐	☒	For null hypothesis testing, the test statistic (e.g. *F*, *t*, *r*) with confidence intervals, effect sizes, degrees of freedom and *P* value noted *Give P values as exact values whenever suitable.*
☒	☐	For Bayesian analysis, information on the choice of priors and Markov chain Monte Carlo settings
☐	☒	For hierarchical and complex designs, identification of the appropriate level for tests and full reporting of outcomes
☐	☒	Estimates of effect sizes (e.g. Cohen's *d*, Pearson's *r*), indicating how they were calculated

Our web collection on statistics for biologists contains articles on many of the points above.

Software and code

Policy information about availability of computer code

Data collection	Equipment software of Applied Biosystems 7300 real-time PCR unit, FACS Aria2, Illumina HiSeq2500, Illumina NovaSeq and Super-ressolution microscope Zeiss LSM 880
Data analysis	Image J(v2), Flowjo (v10), Microsoft Excel (v16), R Studio (v3.4), Cutadapt (v1.18), Samtools (v1.9), Bedtools (v2.26.0), DeepTools (v3.1.0), IGV (v2.3.92), HISAT2 (v2.1.0), Rsubreads (v1.26.0), DESeq2 (v1.10.0), DisgeNET (v5.0), PANTHER (v14.1), Picardtools (v2.17), Bowtie2 (v2.2.6), MACS2 (v2), GREAT (v3.0), seqMiner (v1.3.4), HOMER (v4.8), BETA (v1.0.7), NucleoATAC (v0.3.4), pyDNase (v0.2.4), Juicer (v1.5.2), Fit-Hi-C (v1.1.3), HiCCUPS (v1.7.6).

For manuscripts utilizing custom algorithms or software that are central to the research but not yet described in published literature, software must be made available to editors/reviewers. We strongly encourage code deposition in a community repository (e.g. GitHub). See the Nature Research guidelines for submitting code & software for further information.

Data

Policy information about availability of data

All manuscripts must include a data availability statement. This statement should provide the following information, where applicable:

- Accession codes, unique identifiers, or web links for publicly available datasets
- A list of figures that have associated raw data
- A description of any restrictions on data availability

Data can be accessed at the GEO repository using the accession number GSE125068

Field-specific reporting

Please select the one below that is the best fit for your research. If you are not sure, read the appropriate sections before making your selection.

☒ Life sciences ☐ Behavioural & social sciences ☐ Ecological, evolutionary & environmental sciences

For a reference copy of the document with all sections, see nature.com/documents/nr-reporting-summary-flat.pdf

Life sciences study design

All studies must disclose on these points even when the disclosure is negative.

Sample size	In NGS experiments no statistical methods were used to pre-determine sample sizes but our sample sizes are similar to those reported in previous publications (Mo et al. 2015, Neuron 86, 1369-84). Sample size was estimated according to data variance and correlation between biological replicates and distance to control condition. Each analysis was done in accordance to the sample size, sequencing depth and conditions.
Data exclusions	No data was excluded from the analyses
Replication	Reproducibility across replicate was very high. The measures applied to evaluate replicates were correlation among samples, variance, Euclidean classification, principal component analysis (PCA) and statistical tests that revealed non significant differences within the group. In the analyses in which a replicate was not available, analyses were supported by the use of internal controls and the sample was normalized and compared with samples from related conditions in which replicates were available (i.e., ANOVA, Desq2).
Randomization	Set of mice with the same age and sex were raised in the same conditions and randomly allocated to the different experimental groups.
Blinding	Blinding was not applied in the study because animals need to be controlled by treatment conditions.

Reporting for specific materials, systems and methods

We require information from authors about some types of materials, experimental systems and methods used in many studies. Here, indicate whether each material, system or method listed is relevant to your study. If you are not sure if a list item applies to your research, read the appropriate section before selecting a response.

Materials & experimental systems

n/a	Involved in the study
☐	☒ Antibodies
☒	☐ Eukaryotic cell lines
☒	☐ Palaeontology
☐	☒ Animals and other organisms
☒	☐ Human research participants
☒	☐ Clinical data

Methods

n/a	Involved in the study
☐	☒ ChIP-seq
☐	☒ Flow cytometry
☒	☐ MRI-based neuroimaging

Antibodies

Antibodies used	α -NeuN (1:2000, Chemicon MAB377), α -GAD67 (1:800, MilliporeMAB5406), α-Fos (1:500, Synaptic Systems 226004), α-GFP (1:1000, Aves LabsGFP-1020), α-Fos-Alexa647 (1:40, sc-52 AF647), a-Guinea Pig IgG (H+L) Alexa 594 (1:400, ThermoFisher #A-11075), anti-H3K4me3 (5 µg/ChIP, Millipore 07-473), anti-H3K27ac (5 µg/ChIP, Abcam ab4729), anti-CBP (10 µg/ChIP, Santa Cruz sc583x) and anti-RNAPII (5 µg/ChIP, Santa Cruz sc901x).
Validation	All the antibodies used in this study have been validated in mice for the application in which they were used. This can be confirmed in the scientific publications listed in the manufacturers website. In immunostainings we used appropriate negative controls. In ChIP experiments we used ENCODE validated antibodies whenever possible and included pre-immune IgG as a negative control.

Animals and other organisms

Policy information about studies involving animals; ARRIVE guidelines recommended for reporting animal research

Laboratory animals	Experiments were conducted in male mice (mean 4-month old, range from 3- to 6-month old). Mouse strains were maintained in a pure C57BL/6J background. The origin of the different strains are: CaMKIIα-creERT2 (Erdmann et al., 2007; from the European Mouse Mutant Archive EMMA strain 02125), cre-dependent riboTRAP (Stanley et al., 2013; Jackson labs, stock #030305) and Sun-1 tagged mice (Mo et al., 2015; Jackson labs, stock #021039).

Wild animals	The study does not involve the use of wild animals
Field-collected samples	The study does not involve field-collected samples
Ethics oversight	We followed Spanish and European regulations and all protocols were approved by the Animal Care and Use Committees of Consejo Superior de Investigaciones Científicas (CSIC) and Instituto de Neurociencias, UMH-CSIC.

Note that full information on the approval of the study protocol must also be provided in the manuscript.

ChIP-seq

Data deposition

☒ Confirm that both raw and final processed data have been deposited in a public database such as GEO.

☐ Confirm that you have deposited or provided access to graph files (e.g. BED files) for the called peaks.

Data access links *May remain private before publication.*	https://www.ncbi.nlm.nih.gov/geo/query/acc.cgi?acc=GSE125068 GEO accession number GSE125068
Files in database submission	ChIP_Pol2_Sal.fastq.gz ChIP_Pol2_KA1h.fastq.gz ChIP_H3K27ac_Sal_rep1.fastq.gz ChIP_H3K27ac_Sal_rep2.fastq.gz ChIP_CBP_Sal_rep1.fastq.gz ChIP_CBP_KA1h_rep1.fastq.gz ChIP_CBP_KA1h_rep2.fastq.gz ChIP_Pol2_Sal.bw ChIP_Pol2_KA1h.bw ChIP_H3K27ac_Sal.bw ChIP_CBP_Sal.bw ChIP_CBP_KA1h.bw
Genome browser session (e.g. UCSC)	*Provide a link to an anonymized genome browser session for "Initial submission" and "Revised version" documents only, to enable peer review. Write "no longer applicable" for "Final submission" documents.*

Methodology

Replicates	The number of replicates varies among the different NGS techniques. In the case of ChIP-seq experiments, we considered two experimental replicates per group and condition except in the case of the RNA Pol2 antibody
Sequencing depth	ChIP-seq samples were sequenced in Illumina HiSeq2500 in a single-end 50 bp length configuration. All samples showed >90% reads with high quality mapping to mm10
Antibodies	anti-H3K4me3 (Millipore 07-473), anti-CBP (sc583x) and anti-RNAPII (sc901x)
Peak calling parameters	Reads were mapped with Bowtie2 to mm10 genome index. Peak calling was done with MACS2 with default parameters including the input sample
Data quality	Only peaks with and FDR < 1e-5 were used
Software	Samtools (v1.9), Bedtools (v2.26.0), DeepTools (v3.1.0), IGV (v2.3), Bowtie2 (v2.2.6), MACS2 (v2), seqMiner (v1.3.4)

Flow Cytometry

Plots

Confirm that:

☒ The axis labels state the marker and fluorochrome used (e.g. CD4-FITC).

☒ The axis scales are clearly visible. Include numbers along axes only for bottom left plot of group (a 'group' is an analysis of identical markers).

☒ All plots are contour plots with outliers or pseudocolor plots.

☒ A numerical value for number of cells or percentage (with statistics) is provided.

Methodology

Sample preparation	Mice were sacrified by cervical dislocation, hippocampi were microdisected and washed in PBS. Nuclei were extracted after tissue disruption with a dounce homogenizer and purified by density gradient before sorting

Instrument	FACS Aria III (Becton Dickinson Biosciences, USA)
Software	Flowjo v10.
Cell population abundance	The purity of the post-sorted fractions were 98-99% as determined by re-sorting of sorted nuclei and observation in a neubauer chamber
Gating strategy	Nuclei samples were first gated by their DAPI signal, which positioned the SSC-H from 200 to 700, and FSC-H from 200 to 500. Later, singlets were gated in the linear relation between FSC-A and FSC-H. Finally, nuclei were sorted by their positive fluorescent signal of interest. Population boundaries were clearly separated by normal density

☒ Tick this box to confirm that a figure exemplifying the gating strategy is provided in the Supplementary Information.